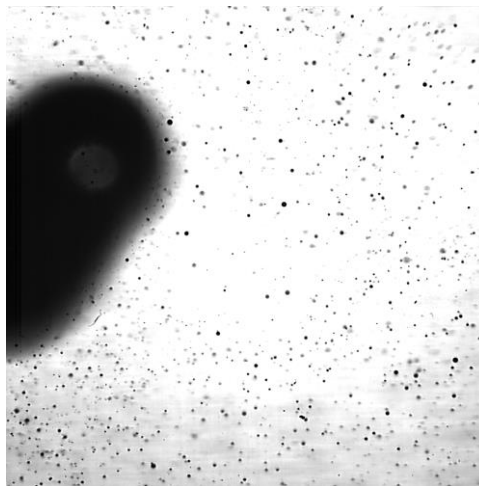FMH606 Master's Thesis 2022
Process Technology

The effect of water spray and mist on the hydrogen-air explosion

Suraj Thapa

Faculty of Technology, Natural Sciences and Maritime Sciences

Campus Porsgrunn

University of South-Eastern Norway

www.usn.no

Course: FMH606 Master's Thesis, 2022

Title: The effect of water spray and mist on the hydrogen-air explosion

Number of pages: 65

Keywords: Hydrogen, Droplet, Mixing chamber, Mist spray

Student:	Suraj Thapa
Supervisor:	Dag Bjerketvedt, Joachim Lundberg
External partner:	MoZEES

Summary:

With the world shifting to greener energy, hydrogen has received more traction than any other alternative fuel in the last decade. With it comes the risk of hydrogen-air explosion. The effects of water mist in explosion energy absorption are not novel. Various study on the use of water mist for the hydrogen-air explosion has been done.

This thesis proposes simple models for droplet evaporation and droplet acceleration under explosion conditions. The models were developed by analyzing various correlations developed so far by other authors, and simplifying the correlations further with elementary assumptions. The models were simulated in python. Models are based on fundamental equations, making them simple for readers.

As part of the thesis objective, a mixing chamber was designed and prototyped for hydrogen-air-mist mixture and tests were done. Furthermore, to understand the interaction between hydrogen-air-mist, the droplet exiting the nozzle was studied. This was done by LASER technique imaging and image processing in ImageJ. The data were further processed to get a trend. It is seen that the droplet diameter changes with exit pipe length.

The model, upon simulation, gave existing trends, generated by already existing models, denoting the feasibility of the model. The prototype also performed its function while exhibiting margin for significant design improvements.

Preface

This report contributes to the final work for the course FMH606 Master`s Thesis of Master of Science – Process Technology at the University of South-Eastern Norway (USN).

This thesis aims to research and analyze the effect of water spray and mist on hydrogen-air explosion by understanding the droplet evaporation rate, droplet acceleration rate, and the droplet characteristic before the explosion.

I would like to thank my supervisor, Professor Dag Bjerketvedt, and my co-supervisor Associate Professor Joachim Lundberg, for the supervision, expert guidance, and helpful insights during the work on this thesis. Alongside, I would also like to take the chance to also thank chief Engineer Øyvind Johansen, for sharing his expert opinion and ideas in the fabrication process, along with Ph.D. scholar Raghav Sikka for his insightful suggestions.

I am also profoundly thankful to my best friends Swostika Thapa, Onkar Prakash Bhujange, and Suzan Samuel for their support throughout this journey.

Finally, I would like to express my humble gratitude to USN, who gave me such a precious chance to study in Norway.

May 31, 2022

Porsgrunn

Suraj Thapa

Contents

List of Figures

1 Introduction

1.1 Background

Discovered in 1766 and identified as a separate element in 1776, by Henry Cavendish, hydrogen is the first element in the periodic table with the atomic number of 1. Despite being the most abundant element in the universe and on the Earth's surface, it is rarely found in the free molecular form because of its extreme reactivity. It can be considered an ideal gas over a wide range of temperatures and even at high pressures. Because of its natural abundance in various forms and environmental friendliness, it has been seen as a great potential energy carrier for smoothing fluctuating renewable energies or for storing excess energy [1],[2].

With hydrogen's potential to be an energy carrier, hydrogen has found new applications. With today's focus on climate change and the transition to greener energy, hydrogen is, by many, seen as one of the major contributors to the transition from fossil fuels to cleaner energy. Along with ammonia production for agriculture and hydrocracking to create petroleum products, hydrogen is currently used as a storage medium, storing excess energy produced from renewable energy sources like wind turbines and hydro powers.

Hydrogen's application in the transportation sector has also increased significantly. The development of a Proton Exchange Membrane (PEM) fuel cell for an electric motor has already taken shape and is still taking further leaps. Furthermore, many countries are also starting to import/export hydrogen cross-continent for practical use. Australia and Japan's agreement to export hydrogen to Japan under the Australian Clean Hydrogen Trade Program (ACHTP) only highlights it [3].

1.2 Problem Description

While hydrogen is getting a lot of traction in the energy sector, with hydrogen's high combustibility, the safety issue is eminent. The risk of hydrogen-air explosion is ever-present, not only in nuclear power plants but also in the process and energy industry [4].

Hydrogen–air explosion is when the hydrogen, in the presence of air ignites, resulting in a rise in pressure. Hydrogen is explosive when mixed with air in a wide range of concentrations and for this reason, can lead from deflagration to detonation fast. This statement is supported by Bjerketvedt D. et al, saying "Hydrogen is very reactive, and a deflagration may accelerate very fast and easily into detonation. Several accidents have been reported where hydrogen clouds are likely to have detonated." [5]. The explosion of the hydrogen fuel station at Sandvika in June of 2019 further highlights it.

To better understand and mitigate this, a lot of studies are ongoing regarding hydrogen explosion safety. One such study includes the use of water mist in the hydrogen-air explosion.

The use of water mist for fire suppression and energy explosion is not new. Studies on the suppression of various hydrocarbon-air mixtures have been studied for years. [6], [2] and [7]

talk about the suppression of fires using water mists. However, the use of water mist in the explosion has more than one effect. If premixed combustion takes place during the spray activation, water mist droplets can have two opposite effects on flame propagation: flame suppression by extracting heat or flame aggravation with turbulence generation [8].

1.3 Objective

The objectives of this thesis are:

- Literature study of the effect of water spray and mist on hydrogen-air gas explosions,
- Develop a theoretical model for droplet vaporization and droplet movement, followed by a simple python simulation of the models,
- Design and prototype development of the mixing chamber for the hydrogen-air-mist mixture,
- Testing of the droplet characteristics exiting the mixing chamber using the LASER technique.

1.4 Limitation

Before getting into the work, it is necessary to understand the limitation of this work. Some of the limitations of this work are:

- The models are developed with a lot of assumptions, rendering the model simple,
- The values used in the python codes are assumed, and not exact. This is down to the fact that the model development and trend plot in python takes precedence over exact value calculation,
- Owning to the time constraints, the secondary dependency of the model on various attributes has been ignored,
- While the simulation results do show trend, it could've been polished if more time was allocated,
- Experimental data, while showing the trend, was insufficient to develop a mathematical model.

2 Relevant Theory

A part of the thesis was to establish simple mathematical models to understand the basic physics behind single droplet evaporation under the effect of the hydrogen-air explosion. Another part was to understand and model the effect of the explosion on droplet velocity. To better model this, various hydrocarbon - air explosions are studied.

2.1 Effects of water mist spray in a hydrogen-air explosion

National Fire Protection Association (NFPA) describes water mist as water spray whose 99% of the droplets have less than 1000 microns. [9]. While the diameter can vary and usually lie in the range of 20 µm to 500 µm, it usually depends on the water pressure, nozzle diameter, and the overall method to create the droplet [10].

Water mist affects flame propagation in more ways than one. When a water mist is sprayed in the fuel-air explosion, one of two things can happen. The droplet can act as a heat sink, thereby acting as a flame suppression mechanism, or the droplet can act as a perturbation, thereby inducing turbulence, resulting in flame acceleration and detonation [8]. This depends on the droplet diameter, velocity, pressure, and so on [8].

The effect of water spray on explosions and fire suppression has been a topic of great interest. A lot of experiments have been conducted in the past, all yielding similar results.

Bjerketvedt et al. [11] conducted a series of experiments and found a multitude of results. The experiments tested multiple nozzle setups, the number of nozzles, and water pressure. While many different results were seen, what remained common was the peak overpressure was reached earlier when the water deluge was introduced [11]. Bjerketvedt et al. [11] attributed the flame enhancement to the water droplet-induced turbulence [11]. As for the overpressure suppression, mixed results were reported between multiple experimental tests.

Wingerden and Wilkins [12], [13] conducted experiments to investigate the effects of water mist in methane and propane explosion in a rectangular box of volume 1.5 m^3. The experiments were performed in the exact setup as that by Bjerketvedt et al. [11]. While they concluded that the water mist can have both the flame enhancement and flame mitigating effect, they also concluded that water droplets needed to break up to be small enough to evaporate in the flame, thereby enhancing the quenching effect [13]. This is in line with the conclusion by Bjerketvedt et al. [11] regarding the droplet break-up and evaporation of finer mist for flame quenching and reduction in explosion pressure.

Boeck et al. [4] researched to check the influence of water mist on flame acceleration. For the given setup of the experiments, they found out that the water mist had a quenching effect, reducing the explosion overpressure in a visible manner [4]. The work by Taileb et al. [14] yielded same results.

While all the above-mentioned experiments were done under different conditions – with varying nozzle diameters, the number of nozzles, droplet diameters, loading density, and

combustion chamber – all the experiments appear to yield a strikingly similar conclusion: smaller water droplets have a positive flame suppression effect in an explosion.

Droplet size is one of the most important parameters in droplet–flame interaction. To understand the effect of water mist spray in an explosion, the effect of flame on each droplet must be studied. In this part of the chapter, we will talk about numerical approaches to understand the effect of flame on a single droplet

2.2 Single water droplet

Droplet size is one of the most important parameters in droplet–flame interaction. To understand the effect of water mist spray in an explosion, the effect of flame on each droplet must be studied. In this part of the chapter, we will talk about numerical approaches to understanding the effect of flame on a single droplet.

2.2.1 Vaporization by conduction

When a droplet is introduced into the flame front, it experiences heat transfer in all three forms. If we consider a thin thermal layer of thermal boundary, there is a heat transfer by conduction between the droplet and the surrounding.

To deduce the mathematical equation for the heat flux, McAllister et al. [15] provide assumptions to simplify the system and the mathematics:

1. Buoyancy is not important. This means the thermal layer is spherical. This allows for a uniform flow field assumption around the droplet
2. Surrounding air is at constant pressure, implying the heat of vaporization and vapor density remain constant during the evaporation process.
3. If the droplet is not at boiling temperature, the droplet is first heated to the boiling point temperature (T_b) before evaporation takes place.

Let's consider a droplet of diameter D, radius r, density ρ, temperature (T_b), and thermal conductivity k in the combustion zone with temperature T_c. Let A be the surface area of the droplet, and in m^2 and T_b be the boiling temperature. δ represents the thermal boundary layer around the droplet, such that:

$$\delta = C \cdot D;$$

(2.1)

All the attributes are in SI unit, and C is a unitless constant.

Heat flux in the droplet is then defined as [15]:

$$\dot{q}_{cond} = kA \frac{(T_a - T_b)}{\delta};$$

(2.2)

If $\dot{q}_{evap}$ is the required heat for the vaporization, then,

$$\dot{q}_{evap} = \dot{m} h_{fg};$$

(2.3)

where h_{fg} is the heat of vaporization, in J/kg.

Also,

$$\dot{m} = -\frac{d}{dt}\left\{\rho\,\frac{4}{3}\pi\left(\frac{D}{2}\right)^3\right\}; \tag{2.4}$$

If we consider conduction to be the only mode of heat transfer, and that all the heat is consumed for evaporation, equating equation 2.2 and 2.3, and combined with equation 2.3 and equation 2.4, we get,

$$-\frac{d}{dt}\left\{\rho\,\frac{4}{3}\pi\left(\frac{D}{2}\right)^3\right\}h_{fg} = kA\frac{(T_a - T_b)}{C\cdot D}; \tag{2.5}$$

Replacing the formula of the surface area of droplet and solving for the rate of change of square of the diameter $\left(\frac{dD^2}{dt}\right)$; we get:

$$\frac{dD^2}{dt} = -\frac{4\cdot k}{\rho\cdot h_{fg}}\frac{(T_a - T_b)}{C}; \tag{2.6}$$

2.2.2 Heat transfer by convection

In most applications, the droplet is injected with a relative velocity with respect to air, creating a convective boundary layer [15]. This gives rise to a convective heat transfer.

The droplet also undergoes convective heat transfer with the surrounding. The convective heat transfer is given by:

$$\dot{q}_{conv} = hAdT; \tag{2.7}$$

Where h is the convective heat transfer coefficient in W/m^2.K, A is the surface area in m^2 and dT is the temperature gradient in K.

In the case of a spherical droplet, h is obtained from Nusselt correlation [15].

$$Nu = \frac{hD}{k} = 2 + 0.4\cdot Re^{1/2}\cdot Pr^{1/3}; \tag{2.8}$$

$$h = \frac{k}{D}\left(2 + 0.4\cdot Re^{1/2}\cdot Pr^{1/3}\right) \tag{2.9}$$

This represents a special case of convection with the droplet falling freely [16]. When the droplet velocity is zero, the Reynolds number becomes zero, reducing the equation to:

$$Nu = \frac{hD}{k} = 2; \tag{2.10}$$

$$h = \frac{2k}{D} \tag{2.11}$$

This signifies that the model also incorporates conductive heat transfer [16].

2.3 Dependence of h on non-dimensional numbers

2.3.1 Prandtl number

Prandtl number is a non-dimensional fluid property and is given by the ratio of kinematic viscosity and thermal diffusivity [16]. For air, it is close to 1, signifying that the thermal diffusivity and the momentum diffusivity are comparable.

$$Pr = \frac{\text{momentum diffusivity } (\nu)}{\text{thermal diffusivity } (\propto)}$$

Lower Prandtl number represents that the thermal diffusiveness of the fluid is high compared to the momentum diffusivity. One such example of a fluid with a lower Prandtl number is liquid metal [16].

The exact opposite can be seen in oil [16]. In the case of oil, the heat dissipation is very slow but the movement (momentum) transfer is relatively high, making its Prandtl number higher than 1.

At 17 degrees, the Prandtl number of pure water is 7.56 [17].

2.3.2 Reynolds number

Reynolds number is a non-dimensional flow property of a fluid and is defined as the ratio of inertia and viscous forces. A smaller Reynolds number signifies that the viscous force is large enough to dissipate disturbances, thereby keeping the flow laminar. However, a higher Reynolds number signifies that the inertial force is significant enough to trigger the disturbance motion, thereby leading to turbulence.

$$Re = \frac{\text{inertia force}}{\text{viscous force}}$$

The dependence of Nusselt number on Prandtl number and Reynolds number for heat transfer has been well documented and tested. While different correlations have been proposed based on different assumptions, and different data sets with different constants, a general correlation can be seen.

$$Nu = f(Re, Pr),$$

Where $f(Re, Pr)$ is given by:

$$f(Re, Pr) = \frac{1}{Z}(A + B \cdot f(Re) \cdot f(Pr))$$

The different values of A, B, x, and y based on various experimental setups are given in Table 2.1.

Table 2.1: Different values of A, B, Z, x and y

Author	A	B	f(Re)	f(Pr)	Z
Vliet and Leppert [1]	$1.2 \, Pr^{0.3}$	0.53	$Re^{0.53}$	$Pr^{0.3}$	1
Whitaker [18]	2	1	$0.4 \, Re^{1/2} + 0.06 \, Re^{2/3}$	$Pr^{2/3}$	1
Ranz and Marshall [18]	2	0.66	$Re^{1/2}$	$Pr^{1/3}$	1
Renksizbulut and Yuen [19]	$1.2 \, Pr^{0.3}$	0.53	$Re^{0.53}$	$Pr^{0.3}$	$(1 + B_{H,f})^{0.7}$

Where $B_{H,f}$ is a heat transfer number, due to blowing.

The details of the use of these correlations can be found in respective references. The detail of the use of correlations by Whitaker can be found in [16].

There is also a strong correlation between heat and mass transfer at intermediate or low Reynolds numbers [20]. One such correlation can be seen between equation (2.8) and equation (2.12).

$$Sh = \left(2 + 0.4 \cdot Re^{1/2} \cdot Sc^{1/3}\right) \tag{2.12}$$

2.4 Experimental Models

Various experimental models have been developed for droplet evaporation. Different models are based on different assumptions and different data sets with different constants. Some of the commonly mentioned models are mentioned below.

2.4.1 Ranz – Marshall Model

Ranz – Marshall investigated the droplet vaporization in a convective flow field for a symmetric spherical droplet The correlation is experiment-based and is without theoretical justification. The experiments are conducted under quasi-state conditions [21].

The heat droplet vaporization correlation is given by:

$m_{convection} = m_{spherical} \cdot f(Re, Pr),$

Where $f(Re, Pr)$ is given by:

$f(Re, Pr) = 1 + 0.3 \, Re^{1/2} Pr^{1/3}$

2.4.2 Sirignano and Abramzon correlation

Sirignano et al. worked on the droplet vaporization model for spray combustion in [22]. They use the gas phase model developed by them to analyze heat and mass transfer in the gas phase near the droplet To account for the convective heat transfer, they implement film theory, which models the heat and mass transfer resistance between the droplet and the surrounding gas by introducing a gas film of constant thickness around the droplet [22].

The instantaneous droplet vaporization model yielded by the extended film model is given by [22]:

$$\dot{m} = 2\pi \overline{\rho_g} \overline{D_g} r_s Sh^* \cdot \ln(1 + B_M) \tag{2.13}$$

And

$$\dot{m} = 2\pi \frac{\overline{k_g}}{\overline{C_{pF}}} r_s Nu^* \cdot \ln(1 + B_T) \tag{2.14}$$

Where,

$\overline{\rho_g}$ = average density, kg·m^{-3}

$\overline{D_g}$ = binary diffusion coefficient, non-dimensional

$\overline{k_g}$ = thermal conductivity of the gas mixture in the film, W·m^{-1}·K^{-1}

$\overline{C_{pF}}$ = average vapor specific heat in the film, J·kg^{-1}·K^{-1}

Sh* and Nu* = non dimensional parameters,

B_M and B_T are called Spalding mass and heat transfer numbers, non-dimensional.

2.4.3 Frössling correlation

Frössling conducted an experiment in the air with Reynolds numbers in the range of 2 to 800. This was done to extend the results by Stefan for the droplet moving in the gas stream. The correlation developed by Frössling is given by [23]:

$$\frac{dm}{dt} = \frac{4\pi r_1 DM}{RT}(P_1 - P_\infty) \cdot \left(1 + 0.276 Sc^{1/3} Re^{1/2}\right) \tag{2.15}$$

2.5 Experimental Models

Droplet acceleration is another important phenomenon in droplet studies. The time spent by the droplet suspended in air is very important for effective droplet vaporization. For this reason, droplet acceleration is another topic of interest.

A droplet dropped in another fluid experiences two major forces as it drops:
1. Viscous drag force
2. Buoyant force

2.5.1 Drag force

When a particle is dropped into the fluid, the droplet starts to accelerate because of gravity. This acceleration causes the particle to speed up, which develops a force in the fluid that resists the motion of the droplet due to its viscous resistance. This force is known as viscous drag force or simply, drag force. Drag force acts in the direction opposite to the motion of the part The viscous drag force is given by [8]:

$$F_d = \frac{1}{8} C_d \cdot \rho_f \cdot \pi \cdot D^2 \cdot (V_f - V_p) \cdot |V_f - V_p| \qquad (2.16)$$

where,

ρ_f = density of fluid, kg·m^{-3}

D = droplet diameter, m

V_g = gas flow velocity, m·s^{-1}

V_p = particle velocity, m·s^{-1}

C_d = coefficient of drag defined as:

$C_d = \frac{24}{Re_p}\left(1 + \frac{Re_p^{2/3}}{6}\right)$ with Re_p given by:

$Re_p = \frac{\rho_g(V_g - V_p)D}{\mu_g}$.

μ is the dynamic viscosity of the gas, in kg·m^{-1}·s^{-1}.

2.5.2 Buoyancy force

When a particle is placed in the fluid, the particle experiences an upward force exerted by the fluid, known as buoyant force. The buoyancy force is given by:

$$F_b = \rho_f \cdot \left(\frac{1}{6}\pi D^3\right) \cdot g \qquad (2.17)$$

Where,

ρ_f = density of fluid, kg·m^{-3}

D = droplet diameter, m

g = acceleration due to gravity, m·s^{-2}

Two other forces acting on a droplet are the Magnus force and Basset force. Magnus force is a lift force that acts on a particle as a result of a spinning motion. Basset force, also known as history force, is a force developed in a particle moving in a rectilinear motion in a fluid and is related to the history of acceleration of a particle [24]. Basset force is the result of a boundary layer development around the droplet due to acceleration [25].

3 Model development and simulation

3.1 Droplet vaporization

A part of this thesis was to model the effect of hydrogen explosion on water mist droplets. To develop the model, certain assumptions were made. Some of the assumptions are:

Assumptions:

1. The droplet is at an ambient temperature. (T_0 ºC)
2. The flame is laminar.
3. There is no detonation. This simplifies the mathematics of droplet breakup.
4. The air is assumed to be dry. This means the only water content in the mixture is from the water mist supplied.
5. Water mist droplets are assumed to be spherical.

General equation:

$$\dot{q}_{cond} + \dot{q}_{conv} = \dot{q}_{mcpdT} + \dot{q}_{evap} \qquad (3.1)$$

where,

$\dot{q}_{cond}$ = heat transferred through conduction, in J·s^{-1}

$\dot{q}_{conv}$ = heat transferred through convection, in J·s^{-1}

$\dot{q}_{mcpdT}$ = latent heat required to heat the water droplet from ambient temperature (T_o ºC) to the boiling point at a given pressure (T_b ºC), in J·s^{-1}

$\dot{q}_{evap}$ = amount of heat required to evaporate droplet, in J·s^{-1}

Let's take a droplet of liquid with diameter D, in m and density ρ, in kg·m^{-3}. Let r be the radius of the droplet, in m.

If m is the mass of the thin film of droplet evaporated, in kg, at time dt, then:

$$m = -4\pi r^2 \, dr \, \rho$$

Then, the rate of mass evaporation is given by:

$$\dot{m} = -4\pi r^2 \, \rho \, \frac{dr}{dt}$$

$$\dot{m} = -4\pi \frac{D^2}{4} \, \rho \, \frac{1}{2} \frac{dD}{dt}$$

$$\dot{m} = -\frac{1}{2}\pi D^2 \, \rho \, \frac{dD}{dt}$$

$$\dot{m} = -\frac{1}{2}\pi D \, \rho \, \frac{1}{2} \frac{dD^2}{dt}$$

$$\dot{m} = -\pi r \, \rho \, \frac{1}{2} \frac{dD^2}{dt}$$

$$\dot{m} = -\pi D \rho \frac{1}{4} \frac{dD^2}{dt} \tag{3.2}$$

Heat transfer to the droplet is given by:

1. Heat transfer through conduction:

$$\dot{q}_{cond} = kA\frac{dT}{\delta}, \qquad \text{where}$$

$$\delta = C \cdot D$$

Combined, we get:

$$\dot{q}_{cond} = kA\frac{dT}{C \cdot D} \tag{3.3}$$

2. Heat transfer through convection:

$$\dot{q}_{conv} = hAdT,$$

where

$$A = \pi D^2$$

$$h = \frac{k}{D}\left(2 + 0.4 \cdot Re^{1/2} \cdot Pr^{1/3}\right)$$

the equation of h includes the conduction heat transfer in it in the constant 2. So, to separate only the convection term, the first part of the correlation has been removed, making it:

$$h = \frac{k}{D}\left(0.4 \cdot Re^{1/2} \cdot Pr^{1/3}\right) \tag{3.4}$$

Combining the equations, we get:

$$\dot{q}_{conv} = \frac{k}{D}\left(0.4 \cdot Re^{1/2} \cdot Pr^{1/3}\right)\pi D^2 dT \tag{3.5}$$

Assuming that the droplet is at an ambient temperature of (T_o), heat transferred to the droplet is used to increase the droplet temperature to the boiling temperature (T_b) and to evaporate the droplet:

1. Heat consumed to increase the droplet temperature to boiling temperature:
$$q_{mcpdT} = m \cdot Cp \cdot (T_b - T_0) \tag{3.6}$$

   Where,

   m is the mass of the droplet, in kg

   Cp is the specific heat capacity of water at constant pressure, in J·kg^{-1}·°C^{-1}

   dT is the temperature difference between the ambient temperature and the boiling temperature, in K.

2. Heat consumed to evaporate the droplet:
$$\dot{q}_{mcpdT} = \dot{m} \cdot h_{fg} \tag{3.7}$$

Combining all the equations (3.1),(3.2), (3.3), (3.5), (3.6), and (3.7), we get:

$$k\pi D^2 \frac{dT}{C \cdot D} + \frac{k}{D}\left(0.4\,Re^{1/2}Pr^{1/3}\right) \cdot \pi D^2 dT = -\pi D\,\rho\,\frac{1}{4}\frac{dD^2}{dt}Cp(T_b - T_0) - \pi D\,\rho\,\frac{1}{4}\frac{dD^2}{dt} \cdot h_{fg}$$

solving for $\frac{dD^2}{dt}$, we get,

$$\frac{dD^2}{dt} = \frac{4 \cdot k \cdot dT}{\rho \cdot (Cp \cdot (T_b - T_0) + h_{fg})}\left(\frac{1}{C} + \left(0.4\,\cdot Re^{1/2} \cdot Pr^{1/3}\right)\right) \tag{3.8}$$

Since the convective heat transfer coefficient is tuned to not include conductive heat transfer when the flow becomes zero, i.e., Reynolds number becomes zero, this model will, henceforth, be addressed as a tuned model.

In a similar fashion, if we consider the original heat transfer coefficient presented by Incorpera et al. [16] and McAllister et al. [15] and model the equation, we get:

$$\frac{dD^2}{dt} = \frac{4 \cdot k \cdot dT}{\rho \cdot (Cp \cdot (T_b - T_0) + h_{fg})}\left(2 + \left(0.4\,\cdot Re^{1/2} \cdot Pr^{1/3}\right)\right) \tag{3.9}$$

Since the original heat transfer coefficient is used, this model will be referred to as an untuned model.

Both these rates of change of square of the diameter of the droplet due to heat transfer are of the form $\frac{dD^2}{dt} = \Phi$, where Φ is a constant.

This can be further represented as:

$$dD^2 = \Phi \cdot dt \tag{3.10}$$

Integrating equation (3.10) from t_0 to t, and D_0^2 to D^2, we get,

$$D^2 - D_0^2 = \Phi \cdot t$$

$$D^2 = D_0^2 + \Phi \cdot t \tag{3.11}$$

This is the D squared law. The value of Φ is dictated by the flame and fuel burning and the droplet property itself.

To find the dependency of the rate of change of droplet diameter($\frac{dD}{dt}$)on initial droplet diameter, we further simplify equation (3.9) to get:

$$\frac{dD}{dt} = \frac{2 \cdot k \cdot dT}{\rho \cdot D \cdot (Cp \cdot (T_b - T_0) + h_{fg})}\left(\frac{1}{C} + \left(0.4\,\cdot Re^{1/2} \cdot Pr^{1/3}\right)\right) \tag{3.12}$$

3.2 Droplet vaporization

To model the equation for droplet acceleration, various assumptions were made. The assumptions are listed below:

1. The droplet is spherically symmetrical.

2. There is no heat transfer consideration between the droplet and the hydrogen-air mixture, and as a result, no droplet motion was brought up it.
3. The droplet is dropped into the H_2-air mixture with a non-zero initial velocity.
4. Magnus force and Basset forces are not included.

If D is the diameter of the droplet,

Let a be the final acceleration of the droplet as a result of multiple forces experienced by it. If m is the mass for the droplet, then, the net force is given by:

$$F_{net} = \sum F$$

$$F_{net} = \text{weight of the droplet} - \text{Drag force} - \text{Buoyant force}$$

$$F_{net} = W_{droplet} + F_d - F_b \qquad (3.13)$$

If $W_{droplet}$ is the weight of the droplet, in N,

$$W_{droplet} = m \cdot g = \rho_p \left(\frac{1}{6}\pi D^3\right) \cdot g \qquad (3.14)$$

Let F_b be the buoyancy force exerted by the gas on the droplet, in N. Then.

$$F_b = \rho_f \cdot \left(\frac{1}{6}\pi D^3\right) \cdot g \qquad (3.15)$$

Drag force (F_d), in N, is given by:

$$F_d = \frac{1}{8} C_d \cdot \rho_f \cdot \pi \cdot D^2 \cdot \left(V_f - V_p\right) \cdot \left|V_f - V_p\right|$$

For our case, the gas is assumed to be in static condition. i.e., $V_f = 0$.

With this assumption in mind, the equation simplifies to:

$$F_d = -\frac{1}{8} C_d \cdot \rho_f \cdot \pi \cdot D^2 \cdot V_p^{\,2} \qquad (3.16)$$

The minus sign signifies the direction of application of force with regards to the motion of the droplet

Combining all the equations from (3.13) through to (3.16), we get:

$$m \cdot a = m \cdot g - \frac{1}{8} C_d \cdot \rho_f \cdot \pi \cdot D^2 \cdot V_p^{\,2} - \rho_f \cdot \left(\frac{1}{6}\pi D^3\right) \cdot g$$

$$\rho_p \cdot \frac{1}{6}\pi D^3 \cdot a = \rho_p \cdot \frac{1}{6}\pi D^3 \cdot g - \frac{1}{8} C_d \cdot \rho_f \cdot \pi \cdot D^2 \cdot V_p^{\,2} - \rho_f \cdot \left(\frac{1}{6}\pi D^3\right) \cdot g$$

Simplifying for a, we get:

$$a = \frac{g(\rho_p - \rho_f)}{\rho_p} - \frac{3}{4D}\frac{\rho_f}{\rho_p} C_d V_p^2$$

$$\frac{dv}{dt} = \frac{g(\rho_p - \rho_f)}{\rho_p} - \frac{3}{4D}\frac{\rho_f}{\rho_p} C_d V_p^2 \qquad (3.17)$$

After a certain time, the forces balance out and the droplet attains a constant velocity, known as terminal velocity.

In this case, a = 0

If V_t is the terminal velocity, in m·s^{-1}, then it is given by:

$$V_t = \sqrt{\frac{4gD(\rho_p - \rho_f)}{3C_d\,\rho_f}} \qquad (3.18)$$

From equation (3.18), it can be seen that $V_t \propto \sqrt{D}$.

3.3 Model simulation

The rate of change of square of the droplet is graphed. The plot shows D^2 on the y-axis against time on the x-axis. Furthermore, the dependence of the rate of change of droplet diameter on initial droplet diameter is plotted.

On droplet acceleration, the relation between droplet velocity with time is plotted, followed by the relation between terminal velocity and droplet diameter.

All the graphs are shown in the result section, under the simulation subchapter, and discussed in depth in the discussion chapter.

For modeling, all the average values are used. The values can be found in their respective code.

4 Mixing chamber

The mixing chamber was designed as part of the thesis work's experimental setup. A part of the thesis entailed an experimental explosion of premixed hydrogen-air explosion in the presence of water mist droplets. The mixing chamber was designed to premix the hydrogen-air with water mist before sending it to the chamber. The chamber needed to fulfill certain functional requirements.

With that in mind, various designs were drafted. In the upcoming subchapter, the design drafts will be extensively discussed.

4.1 Design Process

The design process began with basic functional feature requirements. The initial functional requirements were:

1. Inlet for hydrogen and air
2. Nozzle entry point
3. Hydrogen-air-water mist mixture outlet

Figure 4.1 shows the first design draft. The proposed dimension was 300 mm X 120 mm X 150 mm. The material proposed was polycarbonate for a transparent view. After initial testing, the chamber would be made from a single sheet of polycarbonate, bent into a rectangular shape instead of multiple surface connections. This would eliminate the risk of leakage from the connected edges.
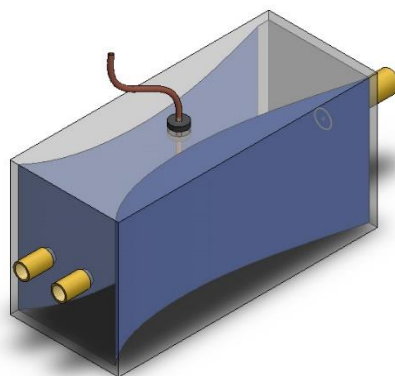

Figure 4.1: First design draft

As seen in Figure 4.1, there were two separate inlets, one for air and the other for hydrogen. The chamber was rectangular in shape and had a venturi shape within to speed the overall flow. This was done to speed up the flow mid-channel. At the end of the venturi region, in front of the outlet, the nozzle was placed for water mist. This allowed for the high-speed hydrogen and air to mix properly with the mist.

One concern of this model was the proper mixing of hydrogen and air after entering the chamber. Since hydrogen and air were entering separately, it was a concern that they would not mix properly. This problem was addressed in the second design draft.
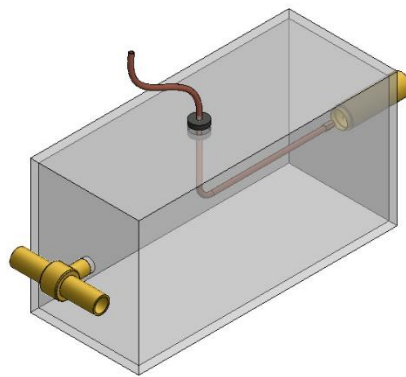

Figure 4.2: Second design draft

Figure 4.2 shows the second design draft. To improve the mixing, perturbations were kept at the choke area of the venturi. This allowed for a high-speed mixture to perturbate and therefore, mix properly. All the other design parameters including the overall dimension and material used were kept the same.

These designs were relatively complex designs from a basic design perspective and prototyping. It required building a venturi shape for a low-pressure region, making the prototyping complex. For this reason, the designs were further simplified.

While the second design draft served the purpose, after consultation and new requirements, a new design draft was created. This is shown in Figure 4.3. As seen in the figure, new features were added.

In the third draft, two major adjustments were done. To begin with, the venturi tunnel and the perturbation were removed. This was done in response to the inlet design change. While the inlet in design drafts one and two was separate for hydrogen and air, in the third design, they were premixed before being sent to the chamber, rendering the use of venturi tunnel and perturbations redundant.

Secondly, a screw opening for the water outlet and volume calculation was added. This was done after studying the nozzle spray angle. While the spray angle was narrow, it was not narrow enough for all the mist to exit. This meant some of the mist would stick to the wall and drip. This further meant that the water mist flow rate from the outlet would not be equal to the water mist flow into the chamber from the nozzle. This difference necessitated the addition of a water outlet.
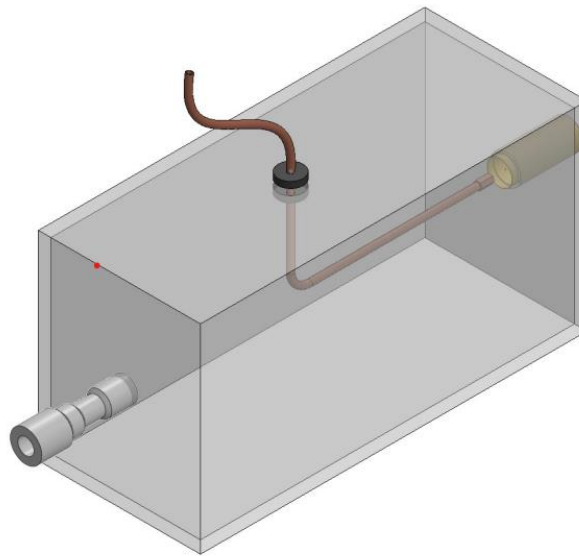
Figure 4.3: Third design draft

Water from the screw would be measured and the difference between the inlet and the collection from the screw mechanism would be measured to calculate the actual mist exiting from the outlet

The third design served all the purposes and met all the requirements. However, a final requirement was added for better flexibility: sliding nozzle inlet This requirement was met in the fourth design draft. During the process, final adjustments were done, and some design features were changed. The cross-section and dimensions of the chamber were some of the most important changes.
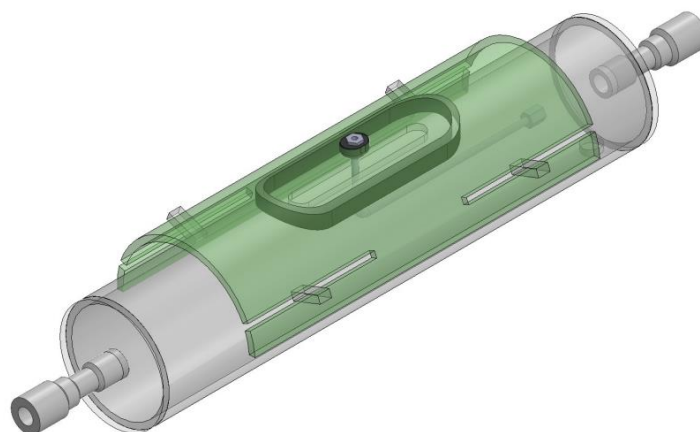

Figure 4.4: Circular cross-sectioned design

Figure 4.4 shows the fourth design of the mixing chamber. As can be seen in Figure 4.4, the cross-section was changed to a circular profile with an internal diameter of 80 mm. This was

done after studying the water mist spray angle. Another reason for the change was the ease of prototyping. While rectangular chamber required bending polycarbonate sheet, inducing a higher chance of creep failure, industry fabricated circular pipe was an easier yet effective prototyping structure.

Another main change was the dimension, brought by the sliding mechanism change. While the initial 300 mm length for previous designs was sufficient for a fixed nozzle setup, the sliding mechanism required extra offset for the nozzle movement inside the chamber. This dictated the latest change in the length of the chamber. The length was changed to 400 mm, with a 100 mm sliding allowance.

A simple sliding mechanism was designed. The design incorporated a 100 mm slot on the surface with a 5 mm thick polycarbonate arc with a diameter of 90 mm sliding on top of it. A rubber gasket was placed in between to seal the mechanism.
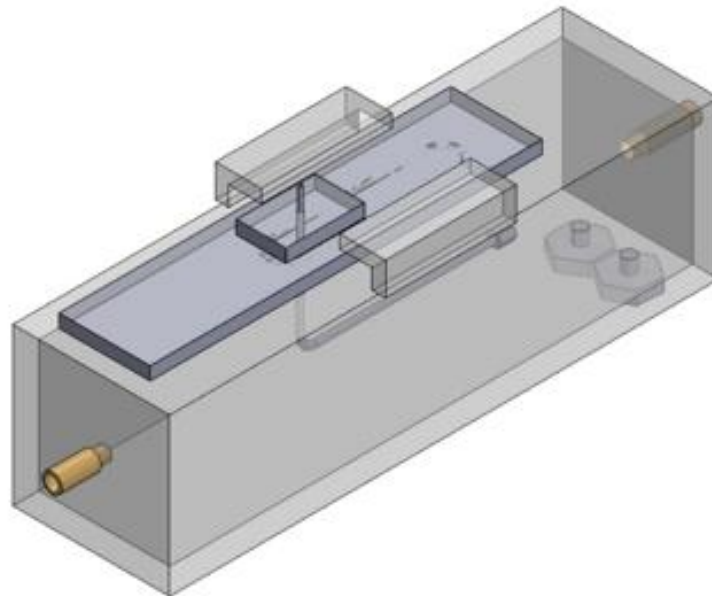

Figure 4.5: Final design draft

While the circular cross-sectional model appeared better on paper, prototyping the design created multiple unanticipated problems.

To begin with, the top sliding surface bent in concave shape. This created a gap between the surfaces, creating a gasket failure.

Another problem faced was the attachment of the slider holder. While the prefabricated circular cross-section reduced a lot of prototyping work, the curved surface was not stable enough for slider holder attachment. This was a major prototyping failure. For this reason, the circular cross-section was abandoned, and the rectangular cross-section was re-selected.

While some minor dimensional changes were made, the essential design remained the same. The final design draft is shown in Figure 4.5. And the features of the design are summarized below:

1. The cross-section was rectangular, with a dimension of 100 mm by 100 mm;
2. 10 mm polycarbonate plates were used.
3. Instead of bending a single plate, they were connected using silicon adhesive.
4. Incorporated a 100 mm slot on the top surface with a 10 mm polycarbonate plate covering it, with a rubber gasket in between.
5. Additional plate on the slider for reinforcement.
6. Smaller hole than the previous design, allowing a better leakage resistance.

4.2 Prototyping

The prototype of the mixing chamber is shown in Figure 4.6. Figure 4.6-a, 4.6-b, 4.6-c, 4.6-d, and 4.6-e show the front, top, side, back, and isometric view of the prototype respectively. 10 mm polycarbonate was cut using a machine cutter according to their design dimensions and glued with multiband silicon adhesive. Silicon adhesive was used primarily to maintain some flexibility in the joints and to address the possible leakage due to the surface irregularities while cutting. To ensure no leakage, the joints were covered with duct tape.

The top surface had a 6 mm thick slot, cut with a milling machine. This was covered by a 12 mm wide gasket Gasket was made from a single rubber sheet of a 5 mm thickness. The gasket slot was handmade.

The entrance was fitted with standard CEJN Brass, stainless steel pneumatic quick connect male coupling, commonly referred to as "Hansen coupling". The entrance plate with Hansen coupling can be seen in Appendix B. The gas–mist exit was fitted with a 10 mm tube. The exit plate with pipe attachment is shown in Appendix C. The pipe was detachable for easy replacement during experiments. An "I" shaped nozzle holder was placed inside the chamber, as part of the design improvisation. This was done to tackle the problem where the nozzle swung around due to its front heaviness. The holder had holes in them to minimize obstruction of the gas flow.

The slider overlaid on the top surface had a rubber attachment on the top surface. The slider clamp, as can be seen in Figure 4.6-b and Figure 4.6-e, clamped the slider at the rubber attachment with two bolts on each side to confirm the final seal. A 4 mm hole was drilled on the slider for pipe entry. As opposed to the 3.2 mm diameter thickness. This was sealed with silicon adhesive on the top surface and tangit on the bottom surface. The slider clamp was fabricated separately and attached using Tangit PVC, a waterproof adhesive.
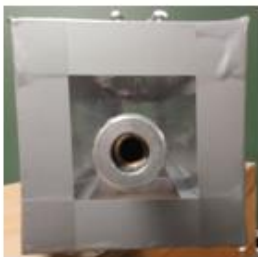
Figure 4.7 shows the in-between fabrication process. The water drainage can be seen in Figure 4.7-a and Figure 4.7-b.
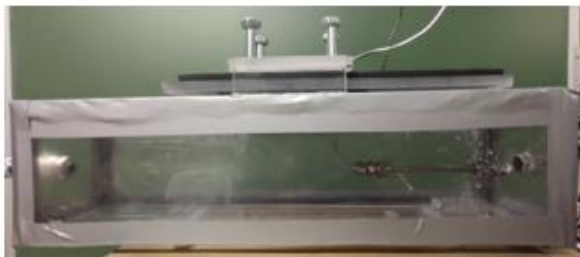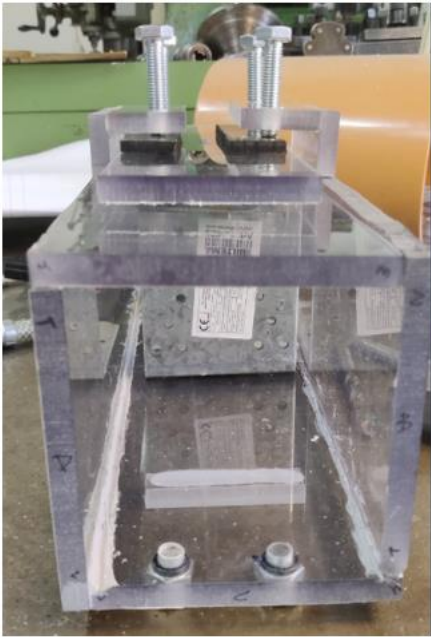
Figure 4.6: Mixing chamber prototype

Figure 4.7: Mixing chamber during mid fabrication process

5 Experiments

In this chapter, we will investigate various aspects of the experiment. The chapter begins with a subchapter with a brief introduction to all the equipment used with their primary technical details. This is followed by another subchapter where all the experimental setups are discussed. This is important because the experimental setup was created in step-by-step form, which is also discussed in the subchapter. The last subchapter talks about the experiments conducted and post-processing done. The results of the experiments can be found in chapter 6, followed by the discussion about the results in chapter 7.

5.1 Model simulation

5.1.1 Camera and software

Photron FASTCAM APX RS was used to film the mist and droplet generation. The camera had maximum frames per second of 250.000 and ran on 1.2 DCV and 6.7 A current. The system ran with an integrated imaging software Photron FASTCAM Viewer software (PFV) Version 3691. It is shown in Figure 5.1.
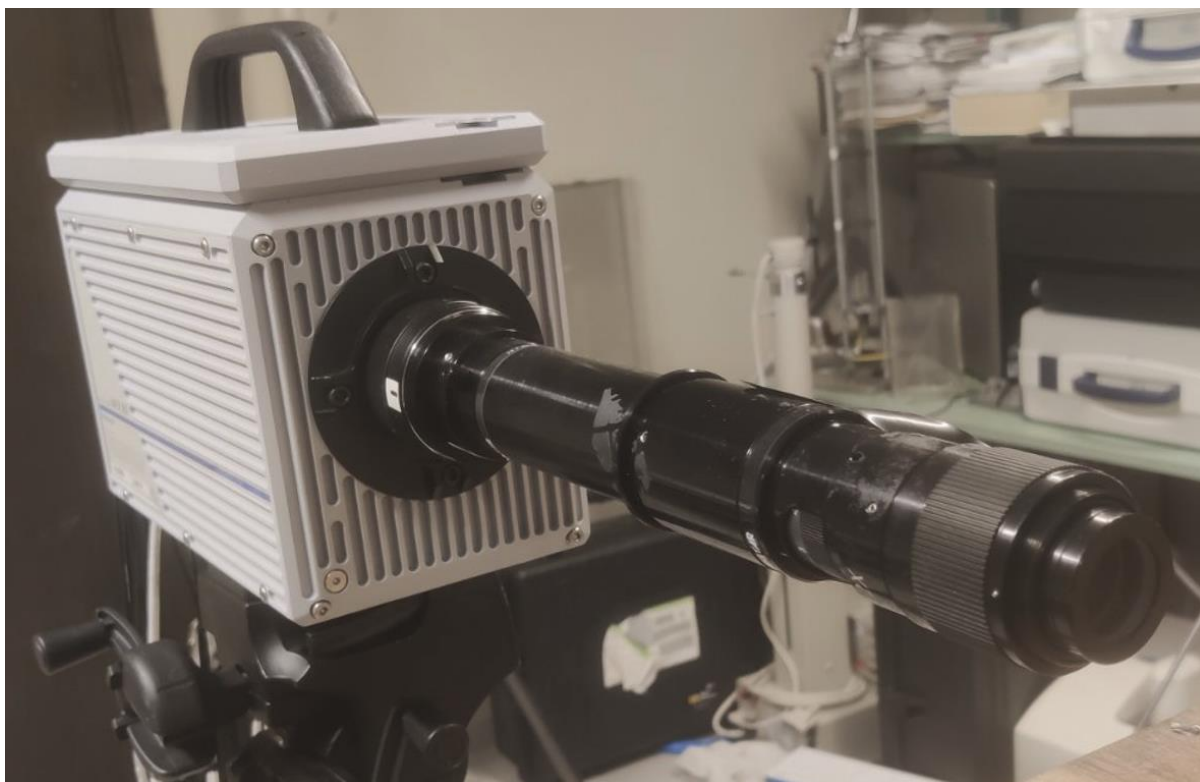

Figure 5.1: Photron FASTCAM APX RS

The camera was setup on a Manfrotto 400 – 3 Geared Pan – and – Tilt Head with Select Quick Release Plates and Manfrotto 161mk2b tripods were used for setup.

Figure 5.2: Figure 1a (on the left) is the Manfrotto 400 – 3 Geared Head [26]; Figure 1b (on the right) is the Manfrotto 161 mk2b tripod [27]

Photron FASTCAM Viewer software (PFV)

Photron FASTCAM Viewer software (PFV) is an image processing software developed by Photron. The software provides a user interface for the camera and allows for a change in frame rate, snipping, shadow correction, image enhancement, data saving, and various other post-processing features.
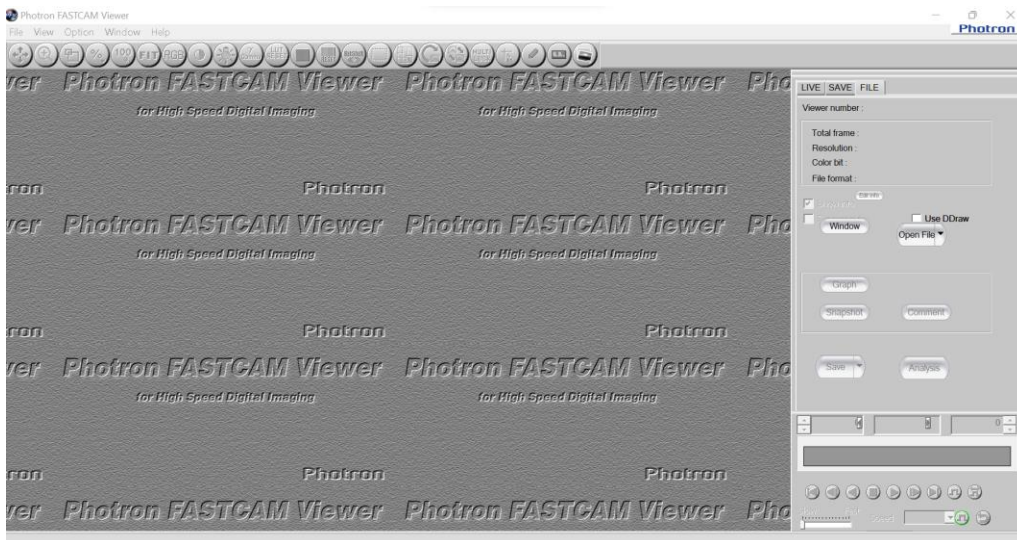

Figure 5.3: Photron FASTCAM Viewer User Interface

5.1.2 LASER

Firefly High Speed Imaging Laser by Oxford Lasers, here-on referred to as firefly laser, a class IV laser was used. It is designed to be used with a high-speed, high-resolution camera, making

it perfect for this application. The LASER uses semiconductor laser with input power of 100 to 240 VAC, 50/60 Hz, and 500 W.

The system was controlled by a separate control unit, with an inbuilt menu, display, and a toggle key to change various options, including duration, separation, number of pulses, pulse delay, and trigger mode. The unit had a $0 - 1$ key for master power.

Figure 5.4 and Figure 5.5 shows the Firefly High Speed Imaging Laser and its controller as part of the experimental setup.
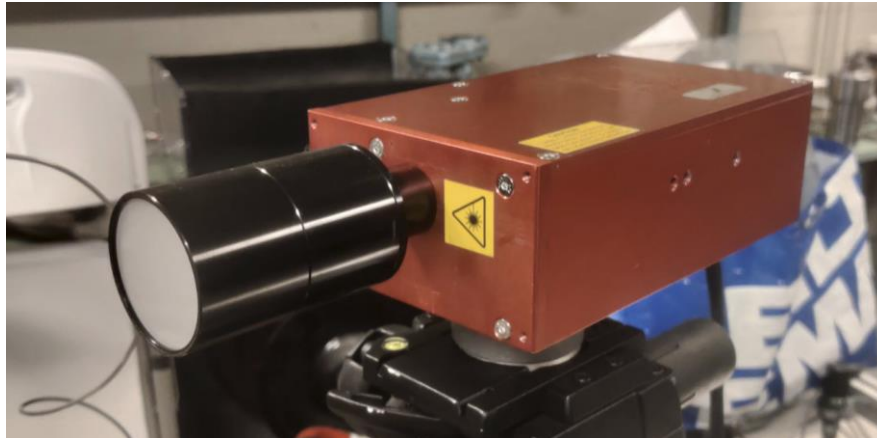
Figure 5.4: Firefly High Speed Imaging Laser

Figure 5.5: Firefly LASER controller

5.1.3 Mist generator

For the initial run, an ultrasonic nozzle by Sono–Tek, U.S.A. was used. Sono–Tek broadband ultrasonic generator was used to control the power in the nozzle, allowing a manual wattage control between 0 and 5 watts, 5.5 being the maximum value. Droplet diameter was regulated by changing the wattage sent to the generator, a higher watt creating finer mist droplets. For a given wattage, The schematic diagram of the mist generator is shown in Figure 5.7 and Figure 5.6 shows the figure of the Sono-Tek nozzle. Further details can be found on their website [28].
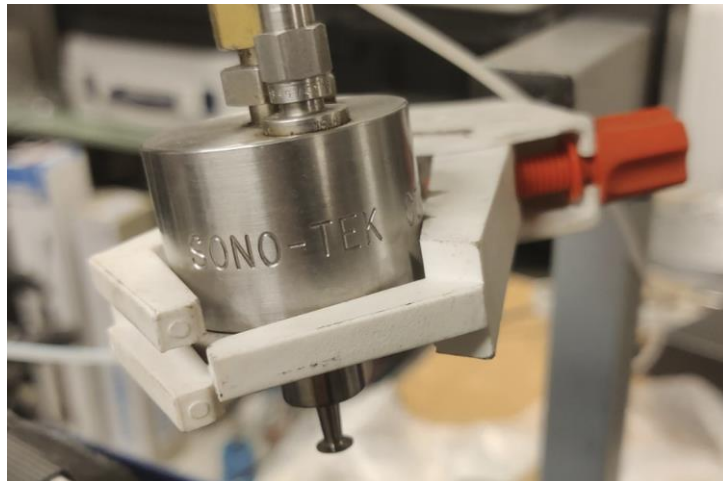
Figure 5.6: Sono-Tek mist generator nozzle
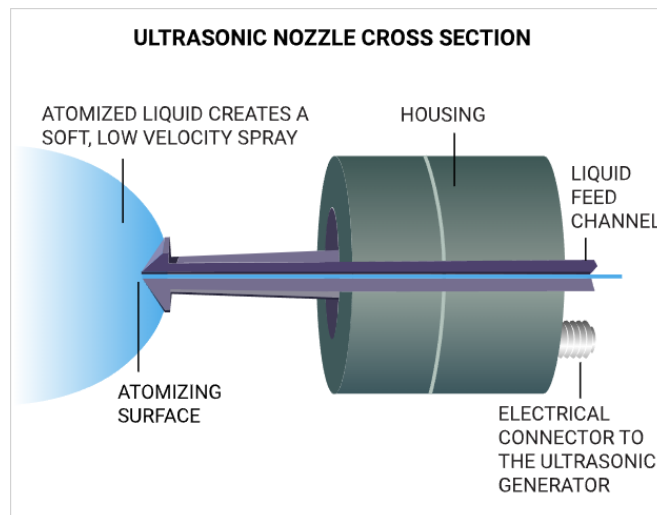
Figure 5.7: Ultrasonic nozzle schematic diagram [30]

For the experiment, the Teledyne ISCO D series pump was used with its pump controller. The pump works on a single geared compressor with a pump capacity of 508 ml, controlled by a D-Series pump controller, shown in Figure 5.8 and Figure 5.9 shows the control panel and the pump and controller set as an experimental setup. Further detail and working of the system can be found in the Teledyne ISCO pump [29].

Figure 5.8: Teledyne ISCO pump controller

Figure 5.9: Teledyne ISCO pump and controller

5.1.4 LED

The test was done using RJ – 45 connector MultiLED QT LED light by SEROF with an active heatsink and 2 fans as the light source. The rated power and supply voltage was 150 W and 48 V and had 120000 Lumen [30].

Figure 5.10: RJ – 45 connector MultiLED QT LED light by SEROF

5.1.5 ImageJ

For the post-processing of the image, ImageJ freeware, 64-bit 1.8.9_172 version was used. The reason for the software selection was the simpler user interface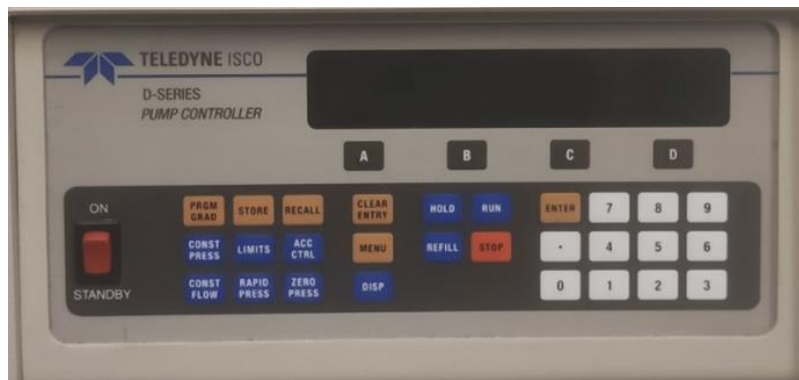, easy learning curve, and accuracy delivered by the software, as verified by the research community. The User Interface of the system is shown in Figure 5.11.
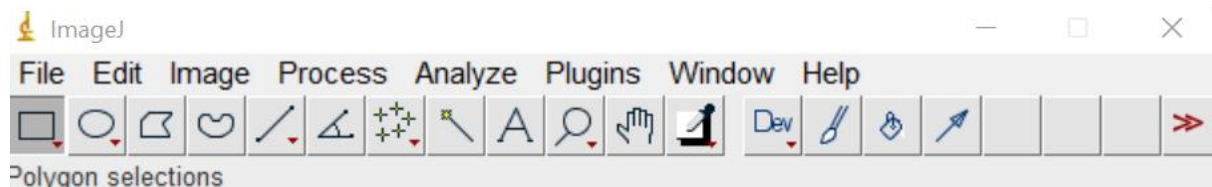
Figure 5.11: ImageJ User Interface

5.2 Experimental setup

The experimental setup and work for the thesis work was conducted in hydrogen explosion laboratory, at USN, Porsgrunn. For the initial test setup, a primary mist generator was used for droplet and mist generation. This part of the chapter is dedicated to explaining the setup, both testing and experimental. Various equipment used during various experimental setups will also be discussed.

5.2.1 Base setup

Base setup was created to set the camera focus, camera zoom, setup alignment and to test the reference dimension for post-processing. The base setup is shown in Figure 12. The camera and light were kept across each other, with a slider mounted in between them. To begin with, a reference glass plate was used as a reference for the camera setup, particularly zoom and

focus. However, the ball was too big to set the reference image. Therefore, the reference was changed to a needle syringe tip of diameter 0.8 mm, for focus and a reference scale glass plate with a minimum reading of 25 microns for scaling. The needle tip was used throughout the experiments for recalibration of the system.

During the first three trials, the light source was kept on the same side as the camera. Although good enough, the setup was too sensitive to the light source movement. Therefore, the LED was kept across the camera and an A3 paper was used to diffuse the light. Both the setup, without and with a diffuser, is shown in Figure 5.12a and Figure 5.12b respectively.

Figure 5.12a: Base setup, without an A3 paper as a diffuser
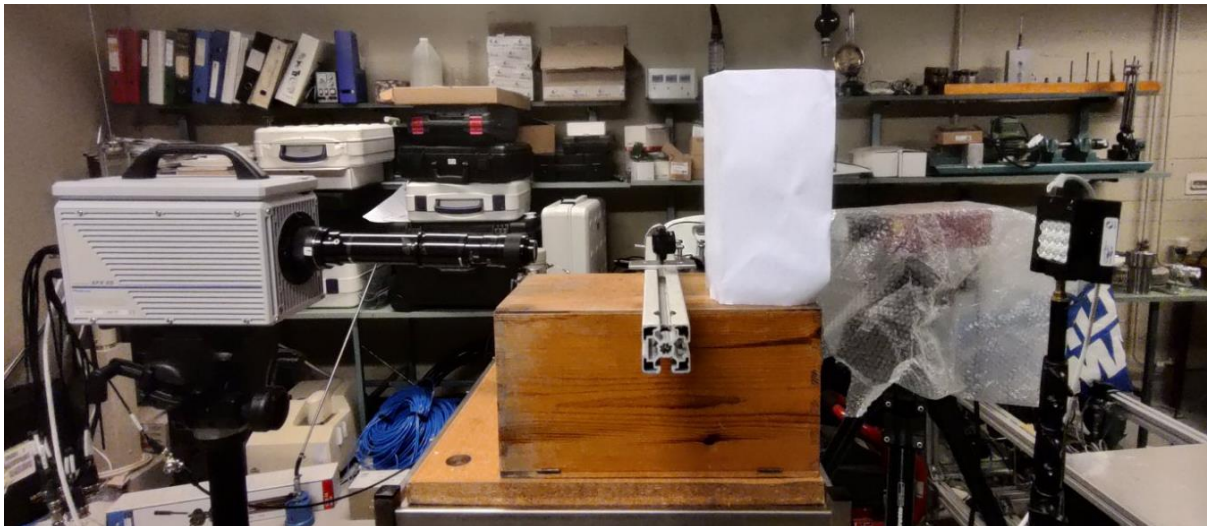
Figure 5.12b: Base setup, with an A3 paper as a diffuser

5.2.2 Test setup

For the test setup, Sono-Tek mist generator was used for mist generation. The camera setup was kept unchanged, and the reference scale was kept constant. LED was replaced with LASER, kept across the camera, with the mist generator placed in between them. The mist

generator was kept perpendicular to the camera – LASER plane. The test setup is shown in Figure 5.13.
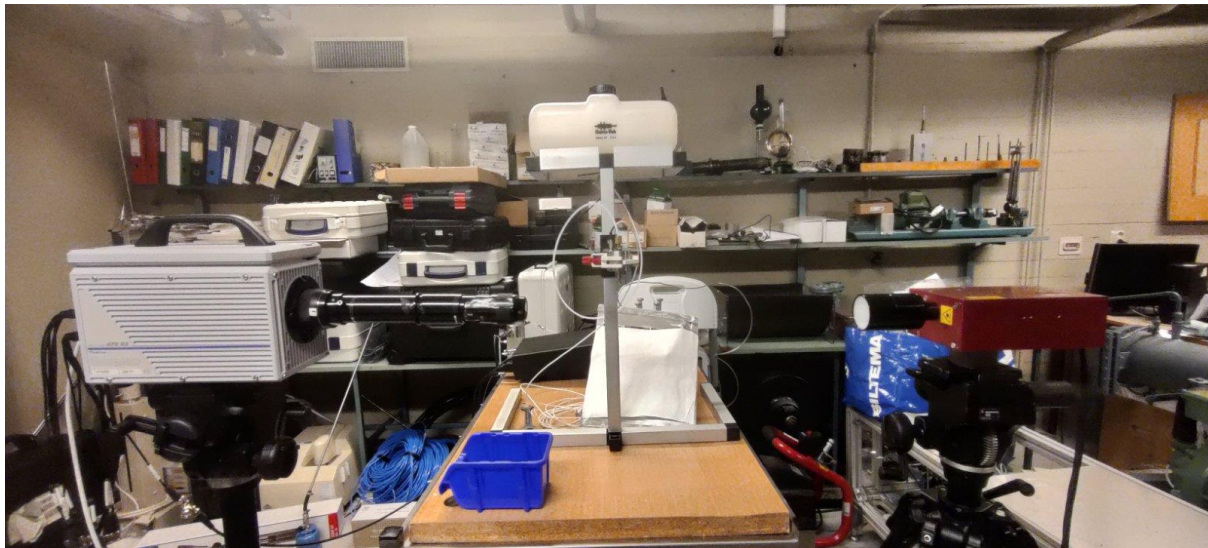
Figure 5.13: Test setup

5.2.3 Experiment setup

For the experimental setup, mixing chamber prototype was the topic of interest. The test setup was kept unmoved, with only the Sono-Tek mist generator replaced with the mixing chamber outlet, connected to Teledyne ISCO 5000 model single-cylinder, single syringe pump with D series pump controller with Swagelok 316L connectors. The total admissible volume was 508 ml with an automatic refill system. The system provided flexibility by working on a constant pressure–variable flow or constant flow–variable pressure mode. The block diagram of the experimental setup is shown in Figure 5.14. Figure 5.15 shows the actual experimental setup from the laboratory.
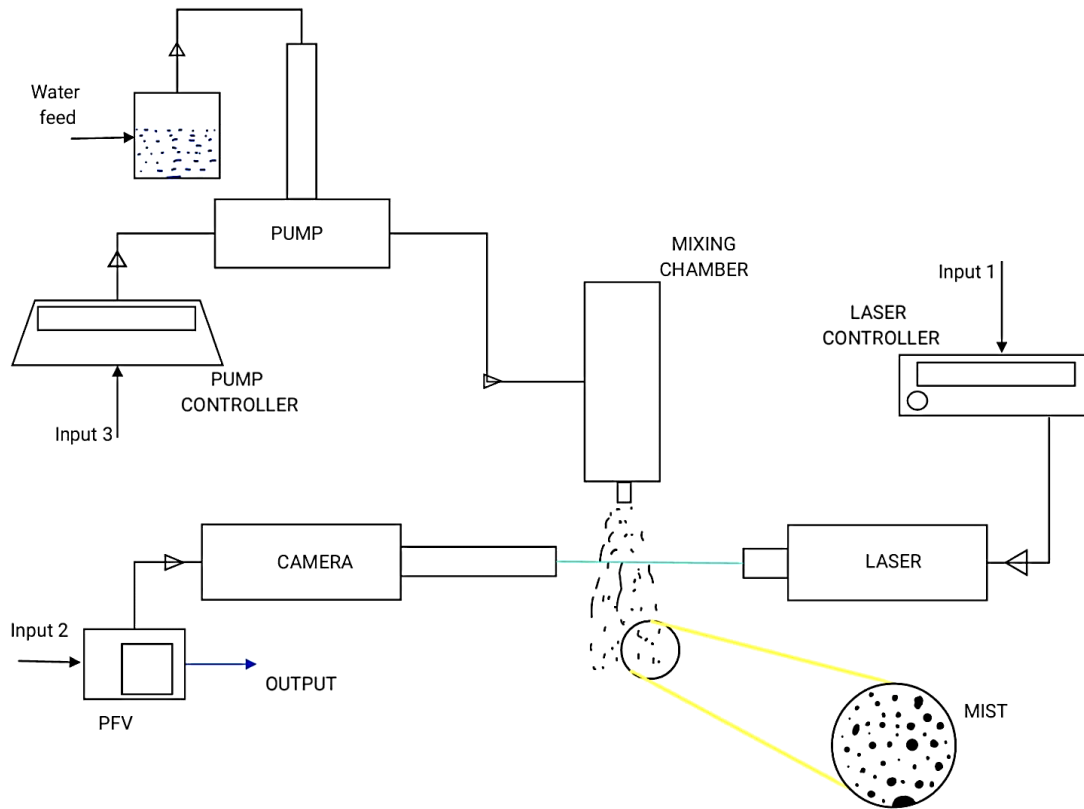
Figure 5.14: Block diagram of the experimental setup
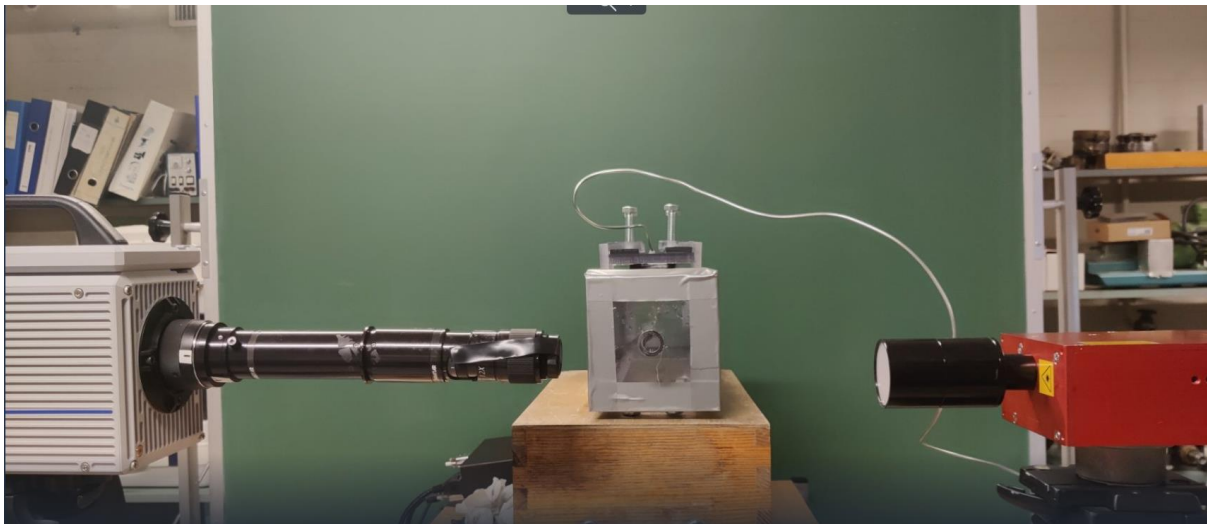
Figure 5.15: Experimental setup

5.3 Experiments

In this subchapter, only the main experiments conducted will be discussed. Furthermore, the test experiments will not be talked about. This is because, the test experiments, while very important for the learning process, did not contribute to the thesis from a results point of view.

As the third task dictated the flow of hydrogen air water mist mixing in the chamber, it was first necessary to see the droplet density at the exit of the chamber. Various experiments were conducted. Three main parameters were changed: outlet pipe length, distance from the outlet surface, and volumetric flow from the nozzle.

During the prototyping, the outlet pipe was designed and prototyped to be detachable and/or replaceable. This design feature was used in the experiment to change the exit pipe length, i.e., the experiment was done with the exit pipe and without the exit pipe attachment. This was done to see how much of the water mist was sticking to the wall in the same experimental scenario and its effect on the mist spray cone angle and distance of the spray.

Initially, the reference scale was set. The scaled image is shown in Figure 5.16. Based on this scale set, the results are produced and post-produced.
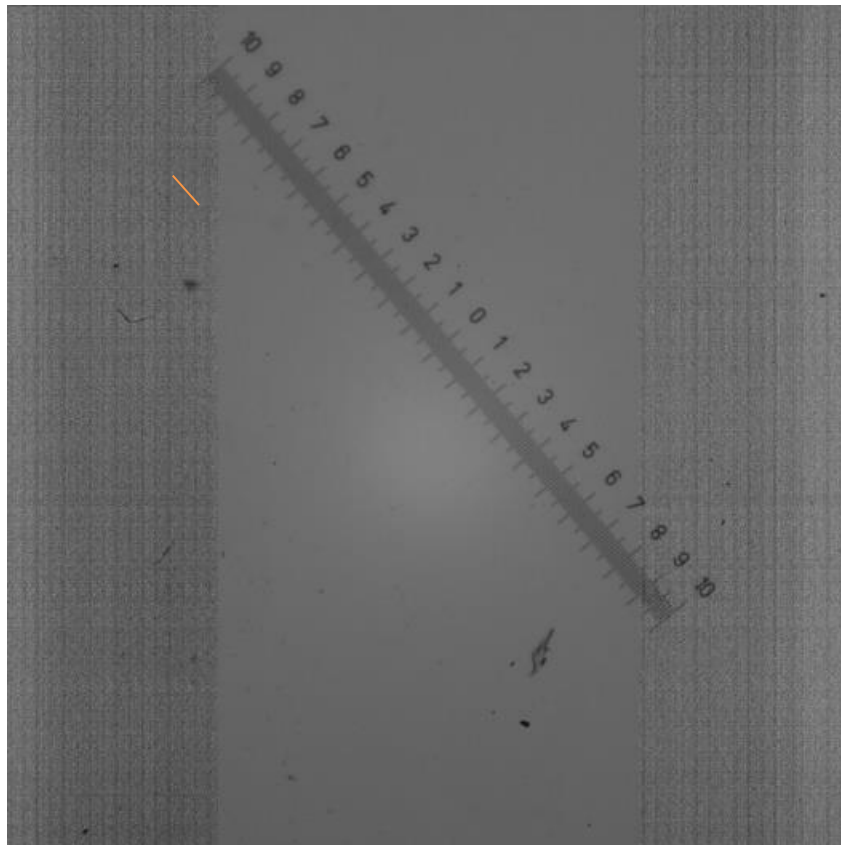
Figure 5.16: Scaled image used for image processing reference

Thereafter, the experimental setup was created. The droplet density was measured at two locations: 25 mm, and 50 m from the outlet orifice in both scenarios i.e., with and without pipe exit. All these were done for three different constant volumetric flow rates: 100 ml/min, 125 ml/min, and 150 ml/min.

The constant pressure–variable flow was also attempted. Using that mode meant the flow output would change over time, meaning the water outlet at any given time was not constant, thus rendering any mist outflow calculation invalid. The idea of constant pressure was therefore suppressed.

12 different experiments were conducted with 2050 images each to see the effect of the nozzle on the exit droplet diameter and the cone angle. Droplet diameters and the number of droplets were measured at 25 mm and 50 mm from the outlet orifice at three different flow rates of 100 ml/min, 125 ml/min, and 150 ml/min each with and without the exit pipe. The images were processed in ImageJ freeware in the bulk of 2050 and the average data were taken.

Table 5.1 shows the systematic way the experiments were done. Figure 5.17 shows the schematic drawing to represent the distance from the outlet orifice (∂). The results were, in the very order, post-processed using ImageJ. The post-processing steps of the spray images are shown in image 5.18. 5.18-a, 5.18-b, and 5.18-c represent the raw image, processed image, and visual result of a single sample image, respectively.

Table 5.1: Experimental data flow sheet

Outlet pipe attachment	Distance from the outlet orifice (∂), in mm	Volumetric flow rate
Yes	25	100
Yes	25	125
Yes	25	150
Yes	50	100
Yes	50	125
Yes	50	150
No	25	100
No	25	125
No	25	150
No	50	100
No	50	125
No	50	150
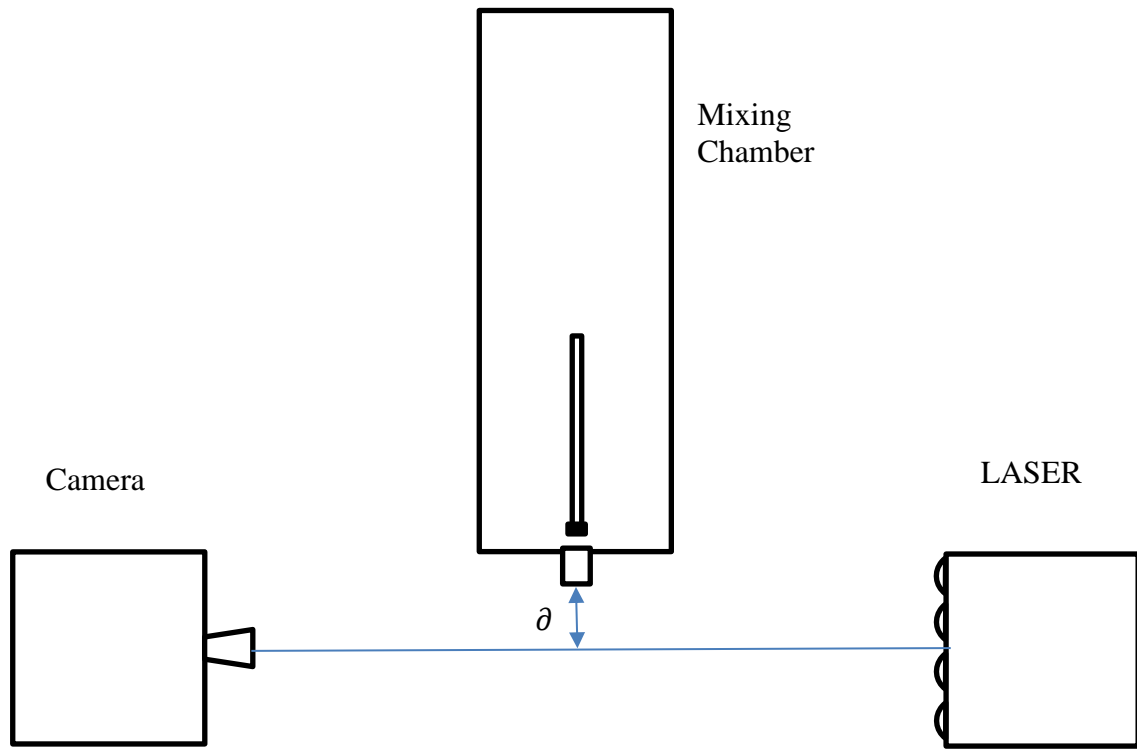
Figure 5.17: Basic setup for outlet distance measurement
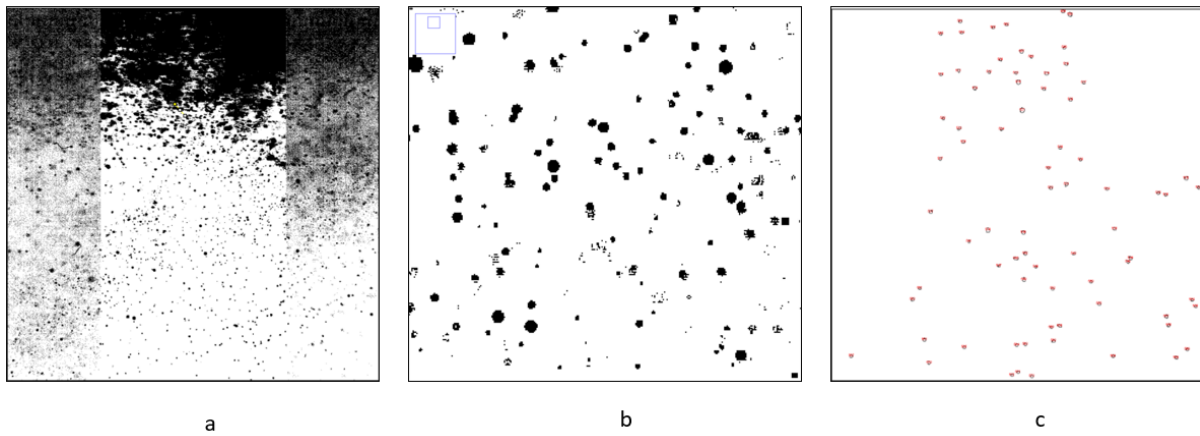
Figure 5.18: Post-processing steps of images in ImageJ

6 Results

6.1 Modeling simulation

Figure 6.1 shows the relation between the square of droplet diameter, on the y-axis and time, on the x-axis for the tuned model. Three different droplet diameters have been simulated, blue, orange, and green representing 100 microns, 150 microns, and 200 microns respectively.
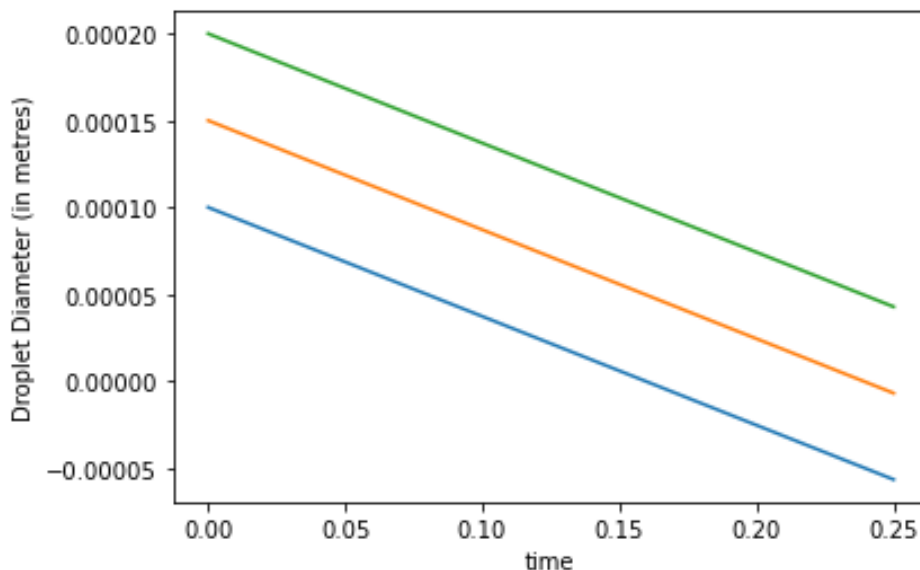
Figure 6.1: A tuned model for multiple droplet diameters

Figure 6.2 shows the relation between the tuned and untuned models. The relation between the square of droplet diameter, on the y-axis and time, on the x-axis for both the tuned and untuned model has been plotted. The code of this simulation can be found in Appendix D.
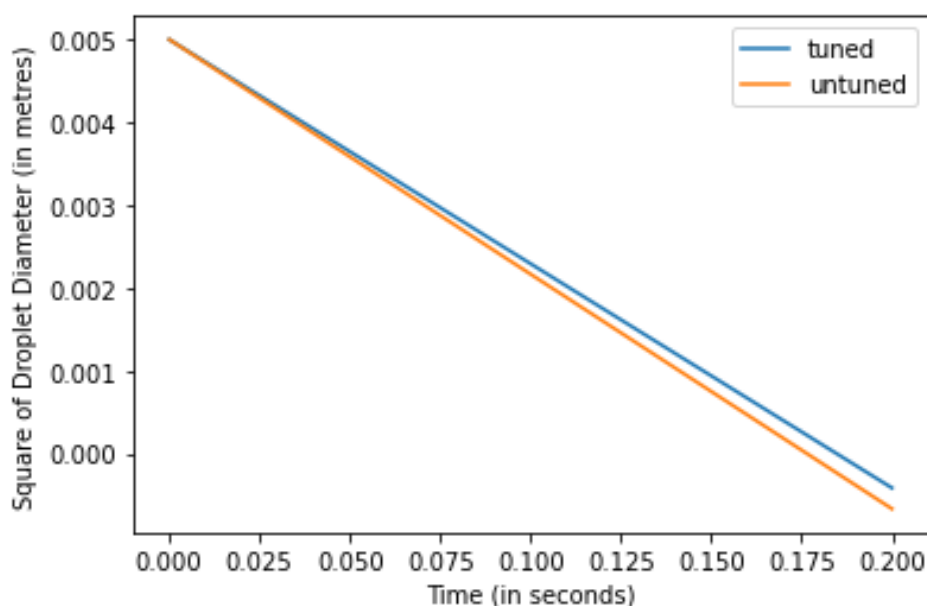
Figure 6.2: Tuned and untuned model

Figure 6.3 shows the relationship between the rate of droplet evaporation with droplet diameter. Rate of droplet evaporation labeled as $\frac{dD}{dt}$ is on the y-axis, while droplet diameter, in microns, is on the x-axis. The code of this simulation can be found in Appendix E.
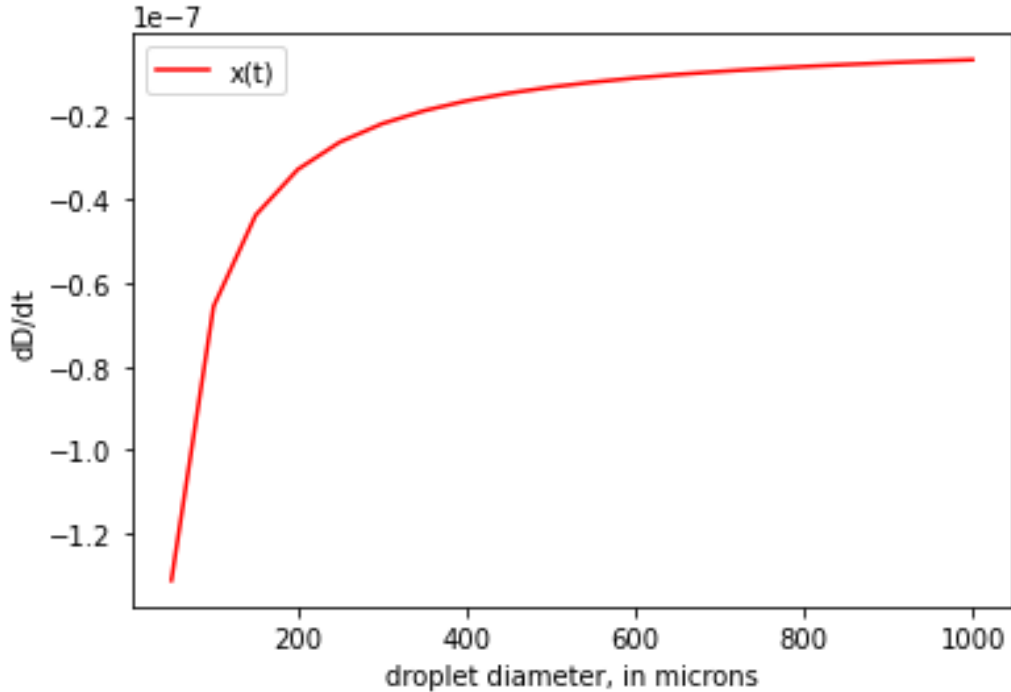
Figure 6.3: Rate of droplet evaporation vs droplet diameter

Figure 6.4 shows the graph plotted between the velocity of the droplet and time. The relation between velocity obtained by the droplet is represented on the y-axis and the timeline is shown on the x-axis. The code of this simulation can be found in Appendix F.
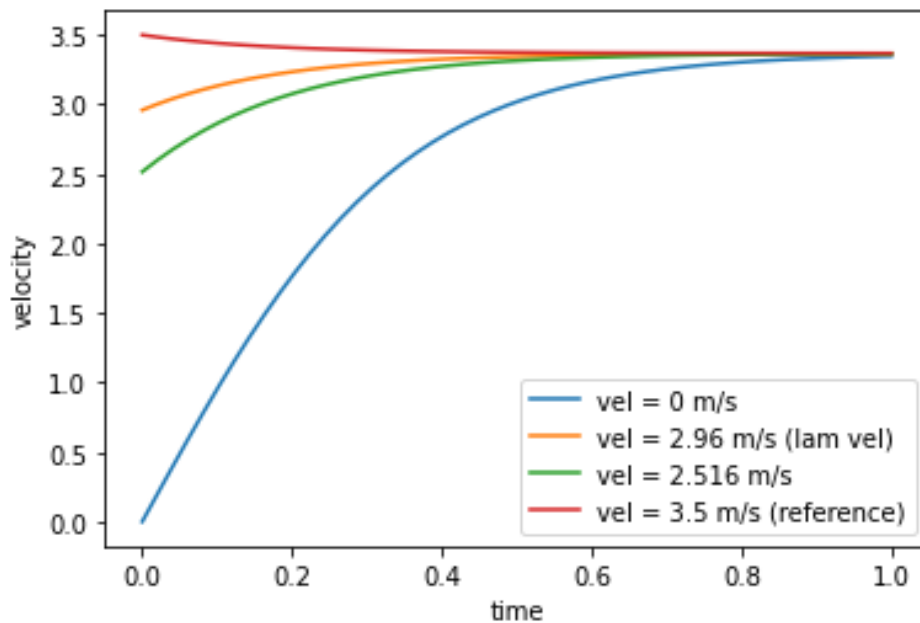
Figure 6.4: Velocity of the droplet vs time

Figure 6.5 shows the dependency of the terminal velocity obtained by the droplet on the initial droplet diameter, in microns. The code of this simulation can be found in Appendix G.
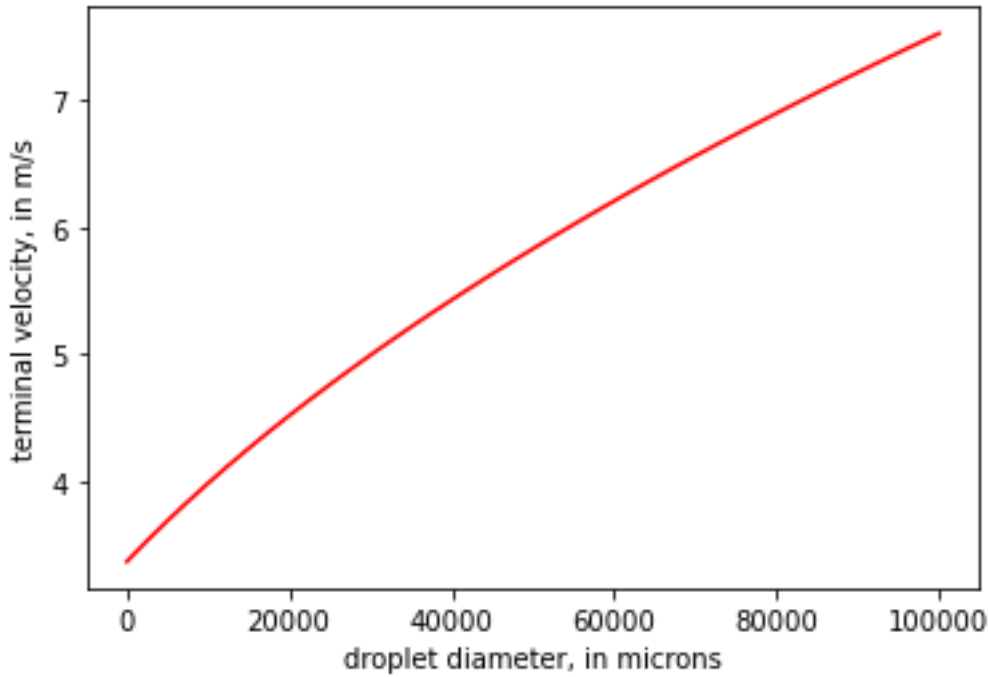
Figure 6.5: Terminal velocity vs droplet diameter

6.2 Experimental results

The result of the experiment has been averaged and shown in Table 6.1. The result is obtained from the droplet area. The calculation has also been done from the droplet perimeter. For results from the droplet perimeter, refer to Appendix H.

Table 6.1: Experimental results

Outlet pipe attachment	Distance from the outlet orifice (∂), in mm	Volumetric flow rate	Area	Diameter	Averaged Diameter
Yes	25	100	1445.394	21.44987	
Yes	25	125	1535.224	22.10637	21.4813
Yes	25	150	1355.607	20.77296	
Yes	50	100	1672.984	23.07689	
Yes	50	125	1618.716	22.69953	22.13871
Yes	50	150	1055.775	18.33231	
No	25	100	1011.038	17.9397	

No	25	125	966.608	17.54109	17.79015
No	25	150	912.137	17.03968	
No	50	100	1094.2	18.66293	
No	50	125	1116.107	18.84883	18.61237
No	50	150	966.237	17.53773	
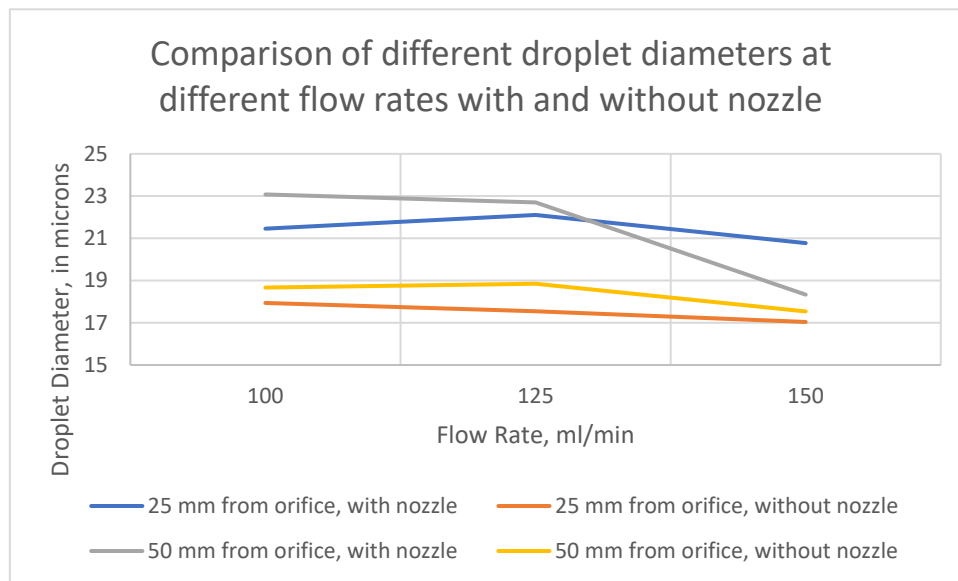
Figure 6.6: Droplet diameter vs the change in flow rate

Figure 6.6 shows the trend of change in droplet diameter with the change in flow rate. First of all, the droplet diameter decreases with the increase in flow rate. To add to that, the droplet diameters appear smaller at a closer distance from the outlet orifice.

Finally, when looking at the set of yellow and grey lines, there appears to be a huge droplet diameter decline due to the presence of the outlet nozzle. The orange and blue lines follow the same trend.
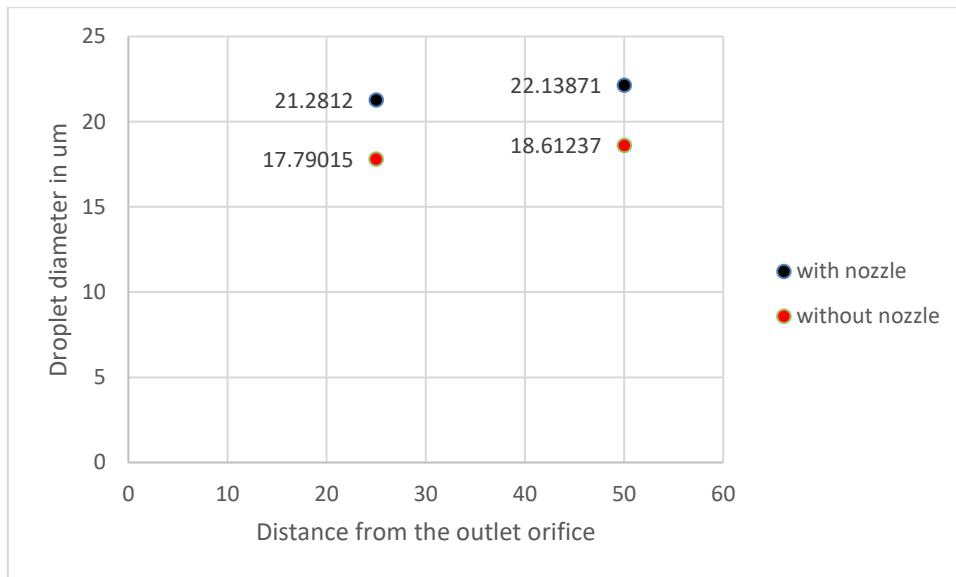
Figure 6.7: Condensed result of the experiment

Figure 6.7 shows the condensed result of the experiment. The red dots represent the averaged droplet diameters of different flow rates at different distances from the outlet orifice without the nozzle. The black dots represent the averaged droplet diameter without the nozzle for different flow rates at different distances from the outlet orifice with the nozzle.

7 Discussion

Different empirical models were studied for the model development. In this chapter, the simulation of the developed model followed by the prototyping & working of the mixing chamber will be discussed. The experimental results from the droplet size study will be explained later.

One of the task descriptions of this thesis was to develop a simplistic model for droplet evaporation. To achieve this objective, previous works were explored. Most works on the topic have been done by correlating data with heat transfer variables[19]. Since most of the models were based on experimental data, the individual effects of conduction, convection, and radiation were rather not clear, especially with models creating various relations with regards to non-dimensional numbers. Most models are developed for droplet fuel evaporation for better combustion. This, combined with the lack of explanation of the effects of individual heat transfer mode in the models, brought up a complicated scenario for model selection. This problem was solved by general equations provided by McAllister et al. [15] for droplet evaporation in both conduction and convection.

The correlation used for the model is based on the work by McAllister et al. [15]. This was adopted because of its simplicity and individual heat transfer relation, which made it easier to underline the effect of both the conduction and convection heat transfer individually and to combine them to create a simplistic, fundamental correlation. While the model is simplistic, it represents the d-squared law, also showing the dependency of the droplet evaporation phenomena on the fuel and droplet property. That being said, the model is still simple, with a lot of physical phenomena not considered. One such example can be seen in the use of the Reynolds number. While keeping the Reynolds number constant, the dependency of the Reynolds number on diameter has been ignored. The consequence of this can be seen when the cases with high and low Reynolds numbers are explored. To be precise, in equation (3.8) and equation (3.9), for a low Reynolds number, the equations remain constant with the Reynold number becoming insignificant. However, for a high Reynolds number, a diameter, raised to the power ½ comes into play. This phenomenon has been ignored. Furthermore, the dependency of C_p, k, and Pr on temperature and pressure has been ignored. This simplicity makes the equation very simple while making it susceptible to error.

Table 2.1 shows various correlations between Nusselt number, Reynolds number, and Prandtl number for a droplet various authors have developed multiple correlations between Nusselt number, Reynolds number, and Prandtl number for convective heat transfer droplet heating within similar scenarios. All the correlations have been experimentally developed and the effects of varying thermophysical characteristics and asymmetrical blowing appear to be treated differently by the correlations [19]. These correlations are usually limited by their limited experimental data [1]. Therefore, these models were not addressed and are presented simply for their acknowledgment.

The correlation by McAllister et al. [15], also mentioned in [16] was chosen to determine the value of the convective heat transfer coefficient. This was further tuned to fit the model and tested against the untuned model. Both the models produced a straight line, representing the form $y = y_0 + kt$, with slight variation in the slope. This can be credited to the difference in the conductive heat transfer part in the model, an untuned model having a constant value of 2, being replaced by (1/C) in the tuned model.

For droplet acceleration, three conditions were simulated: zero velocity, laminar flame velocity, and unburnt flame velocity, represented by blue, orange, and green curves in Figure 6.4. The velocity can be seen increasing, until reaching a final value before settling. All the curves settle at the same point simply because all three curves are plotted for the same droplet diameter. Because all the cases showed velocity increment before settling, an arbitrary value, higher than the settling value was run, to show the decrement in velocity before settling. Again, this curve settled at the same line because it was also simulated for the same diameter.

The curves also show the rate at which they settle. For 0 $m \cdot s^{-1}$ velocity, represented by the blue curve, the rate of conversion is aggressive, compared to that for laminar flame velocity, represented by the orange curve.

It also shows that for a given droplet diameter, a setting velocity was obtained for any initial condition, as a result of the force balancing. With high relative velocity, the drag force and buoyancy force become the dominating force, thereby slowing the droplet. However, with low relative velocity, the mass force accelerates the droplet, finally achieving the settling velocity, as is seen in the simulated cases.

As discussed above, for a given droplet diameter, the droplet settles down to a fixed velocity, irrespective of the initial velocity. However, settling velocity changes with droplet diameter, as represented by equation (3.18). Figure 6.5 shows the dependency of terminal velocity, presented on the y-axis against the initial droplet diameter, presented on the x-axis.

The mixing chamber design was done based on the various requirement. While some designs were drafted to improve the functionality, some were drafted to address the new design requirements. While the circular cross-sectional design appeared the easiest one on paper, the fabrication difficulty and unanticipated material features were encountered. The circular cross-sectional design draft prototyped failed due to the curve flexing, meaning the slider crept inwards, developing a huge gap, thereby rendering leakage. This led to the design and fabrication of what is the final prototype used in all the experiments.

The fabrication of the mixing chamber took around 300 hours of work, with multiple design criteria and possibilities extensively explored. For connecting, the surfaces were connected with a surface on top fashion instead of 45° 90 °. Although 45° 90 ° would have given more surface contact, it was not done to reduce the surface processing time, given the fixed time frame. This was further secured by another layer of adhesive, confirming the strength and flexibility were maintained.

The prototype was prone to a few failures, including creeping failure at slider holder joints that were tested mechanically. While the system did show some flaws, it performed well under high-pressure flow. Another main concern was the leakage of the system. This was tested by feeling the water inside the chamber for 24 hours. The system showed no leakage whatsoever. This, however, led to the nozzle holder failure.

The holder failed halfway through the experiment. The failure revealed another major flaw of the system: the fixed nature of the system. The design was a fixed system design with no possibility to change the internal components of the system. While this was not a new revelation, the severity of this was brought to attention by the failure of the nozzle holder. As a result of this, a better, modular design was designed solving all the previous design flaws of the prototype. Due to the lack of time, the new design was not fabricated nor tested; but the design has been admitted in the report and can be found in Appendix I.

The droplet diameter affects the overall result of its effect in the combustion process. For this reason, it is important to study and understand the droplet characteristics exiting the mixing chamber. In this thesis work, we tried to understand the effects of the exit pipe on the droplet characteristics coming out of the chamber.

The experiment was done to understand the characteristics of the droplet exiting from the mixing chamber. The main topic of interest was the effect of the internal surface of the outlet pipe on the droplet size. Twelve different experiments were conducted, which were categorized into four essentially different categories: droplets from the outlet with outlet pipe at 25 mm distance from outlet orifice, droplets from the outlet with outlet pipe at 50 mm distance from outlet orifice, droplets from the outlet without outlet pipe at 25 mm distance from outlet orifice, droplets from outlet without pipe nozzle at 25 mm distance from outlet orifice.

Figure 6.6 shows the droplet diameter under different conditions. A clear result seen is that with the presence of an outlet pipe, the droplet diameter increases. This can be attributed to the water layer formed on the internal wall of the outlet pipe.

With the increase in flow rate, the droplet diameter decreases. This is another interesting observation. One reason for this is the increase in pressure required to obtain higher flow rates. This theory was also validated when the system was run at low flow rates, rendering larger droplet formation. This holds for both with and without pipe.

The experiments also validated the design strength of the mixing chamber, with the system sustaining high-pressure flow during the experimental setup testing.

8 Conclusion

With the world moving toward cleaner energy, hydrogen is on a fast track to being the energy carrier around the world. While the world moves forward with hydrogen as an energy carrier, all this development in hydrogen technology has entailed extensive research in hydrogen storage-use-and-transfer explosion safety. The explosion of Sandvika, as mentioned earlier, underlines this matter.

This thesis highlights the effects of the hydrogen-air explosion on water mist as an attempt to better understand the droplet evaporating mechanism to further the study of hydrogen safety by mist spray. A simple model for droplet evaporation under explosion and droplet acceleration was created. This was done by making several assumptions. From the model, plots relating the square of droplet diameter with time were developed in python. Alongside, the dependency of the rate of change of diameter on initial droplet diameter was also checked and plotted. Similarly, from the droplet acceleration model, the relationship between the initial velocity and rate of change of velocity, along with the relation between droplet diameter and its terminal velocity was developed. The simulation delivered appropriate results, indicating the positive outcome of the model.

Another task in the thesis was to design and prototype the mixing chamber and analyze the droplet characteristics in the mixing chamber outlet. After multiple visits to various design drafts and chamber requirements, a cross-sectional design draft was selected until fabrication problems were encountered, leading to the rectangular cross-sectional design and prototype. The prototype consumed considerably more time than expected, with multi joints bringing the consciousness of a new problem – joint leakage. This was addressed with multiple hours of water testing. The water mist characteristics study exiting the chamber was also done using the LASER technique to film and ImageJ, an image processing software, to post-process. The results showed that the droplet size increases while exiting the mixing chamber. This was because the outlet pipe contributed to the droplet coalescence.

One of the most significant results in the droplet evaporation has been the value of Φ, representing both the conduction and convection in a simpler yet effective way, including the fuel and droplet properties. The model acts as a base for future work, with ease in understanding and modification. This is significant progress in the, relatively novel, theoretical study of water mist in the hydrogen-air explosion.

Another significant result has been the development of the mixing chamber, followed by the successful testing and droplet characteristic analysis. Even though the prototype was not perfect, it created a baseline and acted as a typical prototype, showing areas for design and fabrication improvement.

The droplet characteristic, owing to the existence of an exit pipe was also studied. It was concluded that the droplet diameter increases with the length of the exit pipe.

While some significant outcomes were seen, the work can be furthered for a better understanding of the effects of water mist and spray on the hydrogen-air explosion. The assumption of many attributes as constant and ruling out the secondary dependence of the equation on various aspects, including pressure and temperature simplified the model. This can be looked upon in the future to develop further advanced models, based on the model developed here.

To add to that, while the evaporation model and acceleration model have been derived irrespective of one another, that is not the optimal case. The combination of these would provide further clarity to the overall process and would be a good step for further improvements.

Furthermore, the design of the mixing chamber can be improved. As mentioned earlier, the prototype design revealed room for many new feature improvements, one of them being modularity. An improved design has been presented in Appendix I for consideration. While the current chamber can be used for hydrogen-air-water mist mixing for explosion tests, the newer design suggested can perform significantly better with multiple design features added. The design can be fabricated for future experiments. To add to that, the prototype can be tested for mixing performances, as part of the future work.

The results of droplet characteristics exiting the mixing chamber are conclusive. However, the study deals with one aspect of the mixing chamber based on the exit pipe length. Further experiments can be performed to better understand the effects of various chamber characteristics, including the chamber dimension, the distance of the nozzle from the exit pipe, and hydrogen-air-mist mixing in the chamber.

Lastly, owing to the time limitation, data was not enough to develop a proper mathematical model between the exit pipe length and droplet diameter. This would be a potent step forward in droplet loading density studies.

References

[1]   B. A. FINLAYSON and J. W. OLSON, 'Heat Transfer to Spheres at Low to Intermediate Reynolds Numbers', *Chemical Engineering Communications*, vol. 58, no. 1–6, pp. 431–447, Aug. 1987, doi: 10.1080/00986448708911980.

[2]   C. Joseph-Auguste, H. Cheikhravat, N. Djebaïli-Chaumeix, and E. Deri, 'On the use of spray systems: An example of R&D work in hydrogen safety for nuclear applications', *International Journal of Hydrogen Energy*, vol. 34, no. 14, pp. 5970–5975, Jul. 2009, doi: 10.1016/j.ijhydene.2009.01.018.

[3]   'Australia signs hydrogen export deal with Japan', *Australian Renewable Energy Agency*. https://arena.gov.au/blog/australia-signs-hydrogen-export-deal-with-japan/ (accessed May 31, 2022).

[4]   L. R. Boeck, A. Kink, D. Oezdin, J. Hasslberger, and T. Sattelmayer, 'Influence of water mist on flame acceleration, DDT and detonation in H2-air mixtures', *International Journal of Hydrogen Energy*, vol. 40, no. 21, pp. 6995–7004, Jun. 2015, doi: 10.1016/j.ijhydene.2015.03.129.

[5]   S. Thapa, E. Nilsen, and V. Zangeneh, 'The hazard of fragments in accidental H2 - air explosions.' Nov. 18, 2021.

[6]   T. Parra, F. Castro, C. Méndez, J. M. Villafruela, and M. A. Rodríguez, 'Extinction of premixed methane–air flames by water mist', *Fire Safety Journal*, vol. 39, no. 7, pp. 581–600, Oct. 2004, doi: 10.1016/j.firesaf.2004.05.001.

[7]   H. I. Mahmud, 'Simulation of the Supression of Fires Using Water Mists', Victoria University, Melbourne, Australia, 2016. [Online]. Available: https://vuir.vu.edu.au/id/eprint/31116

[8]   G. Gai, 'Modeling of water sprays effects on premixed hydrogen-air explosion, turbulence and shock waves', 2020.

[9]   J. R. Mawhinney, R. Darwin, and H. Associates, 'PROTECTING AGAINST VAPOR EXPLOSIONS WITH WATER MIST', p. 12.

[10]   B. P. Husted, 'Experimental measurements of water mist systems and implications for modelling i CFD', Department of Fire Safety Engineering, Lund University, Lund, 2007.

[11]   D. Bjerketvedt and M. Bjorkhaug, *Experimental investigation effect of water sprays on gas explosions*. [Online]. Available: https://catalogue.nla.gov.au/Record/1159906

[12]   K. van Wingerden and B. Wilkins, 'The influence of water sprays on gas explosions. Part 1: water-spray-generated turbulence', *Journal of Loss Prevention in the Process Industries*, vol. 8, no. 2, pp. 53–59, Jan. 1995, doi: 10.1016/0950-4230(95)00002-I.

[13]   K. van Wingerden, B. Wilkins, J. Bakken, and G. Pedersen, 'The influence of water sprays on gas explosions. Part 2: mitigation', *Journal of Loss Prevention in the Process Industries*, vol. 8, no. 2, pp. 61–70, Jan. 1995, doi: 10.1016/0950-4230(95)00007-N.

[14]   S. Taileb, J. Melguizo-Gavilanes, and A. Chinnayya, 'Influence of the chemical modeling on the quenching limits of detonation waves confined by an inert layer', Dec. 2019. Accessed: May 31, 2022. [Online]. Available: https://hal.archives-ouvertes.fr/hal-02394614

[15]   S. McAllister, J.-Y. Chen, and A. C. Fernandez-Pello, *Fundamentals of Combustion Processes*. New York, NY: Springer New York, 2011. doi: 10.1007/978-1-4419-7943-8.

[16]   T. L. Bergman and F. P. Incropera, Eds., *Fundamentals of heat and mass transfer*, 7th ed. Hoboken, NJ: Wiley, 2011.

[17]   G. L. Shires, *PRANDTL NUMBER*. Begel House Inc., 2011. doi: 10.1615/AtoZ.p.prandtl_number.

[18]   'Heat transfer Study on flow through and around a porous permeable sphere', p. 15.

[19]   M. Renksizbulut, R. Nafziger, and X. Li, 'A mass transfer correlation for droplet evaporation in high-temperature flows', *Chemical Engineering Science*, vol. 46, no. 9, pp. 2351–2358, 1991, doi: 10.1016/0009-2509(91)85133-I.

[20]   M. Renksizbulut and R. J. Haywood, 'Transient droplet evaporation with variable properties and internal circulation at intermediate reynolds numbers', *International Journal of Multiphase Flow*, vol. 14, no. 2, pp. 189–202, Mar. 1988, doi: 10.1016/0301-9322(88)90005-5.

[21]   S. K. Aggarwal, A. Y. Tong, and W. A. Sirignano, 'A comparison of vaporization models in spray calculations', *AIAA Journal*, vol. 22, no. 10, pp. 1448–1457, Oct. 1984, doi: 10.2514/3.8802.

[22]   B. Abramzon and W. A. Sirignano, 'Droplet vaporization model for spray combustion calculations', *International Journal of Heat and Mass Transfer*, vol. 32, no. 9, pp. 1605–1618, Sep. 1989, doi: 10.1016/0017-9310(89)90043-4.

[23]   G. A. E. Godsave, 'Studies of the combustion of drops in a fuel spray—the burning of single drops of fuel', *Symposium (International) on Combustion*, vol. 4, no. 1, pp. 818–830, Jan. 1953, doi: 10.1016/S0082-0784(53)80107-4.

[24]   'Chapter 2 - Fluid flow and mass transfer on particle scale', p. 69.

[25]   J. B. Joshi *et al.*, 'Computational fluid dynamics', in *Advances of Computational Fluid Dynamics in Nuclear Reactor Design and Safety Assessment*, Elsevier, 2019, pp. 21–238. doi: 10.1016/B978-0-08-102337-2.00002-X.

[26]   'Studio Geared Head', *Manfrotto*. https://www.manfrotto.com/global/studio-geared-head-400/ (accessed May 31, 2022).

[27]   'Super Professional Tripod Mk2 - 161MK2B | Manfrotto Global'. https://www.manfrotto.com/global/super-professional-tripod-mk2-161mk2b/ (accessed May 31, 2022).

[28]   'How Ultrasonic Nozzles Work', *Sono-Tek*. https://www.sono-tek.com/ultrasonic-coating/how-ultrasonic-nozzles-work/ (accessed May 31, 2022).

[29]   'D4-Series Syringe Pumps', p. 338.

[30]   'High speed camera lighting system : MULTILED QT', *Claravision*. https://www.claravision.com/en/produit/high-speed-camera-lighting-system-multiled-qt/ (accessed May 31, 2022).

APPENDIX A: Task Description

University of South-Eastern Norway
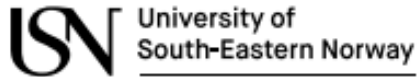
Faculty of Technology, Natural Sciences and Maritime Sciences, Campus Porsgrunn

FMH606 Master's Thesis

Title: The effect of water spray and mist on hydrogen-air explosions

USN supervisor: Prof. Dag Bjerketvedt and Asc. Prof. Joachim Lundberg

External partner: MoZEES (www.mozees.no)

Task background:
Water sprays are effective in mitigating strong gas explosions in hydrocarbon-air clouds. However, the effect of water spray and mist on hydrogen-air gas explosions is not fully understood. Since hydrogen is becoming an important energy carrier in the transition from fossil fuels to green energy, this is an area of significant importance.

Task description:

1. Perform a literature study on the effect of water spray and mist on hydrogen-air gas explosions

2. Model the acceleration and the evaporation of water droplets in a laminar premixed hydrogen-air flame

3. Apply laser techniques to investigate loading density of water and droplet size distribution in spays and mists

Student category: EET, or PT students

Is the task suitable for online students (not present at the campus)? No (Task 1 and 2: Yes)
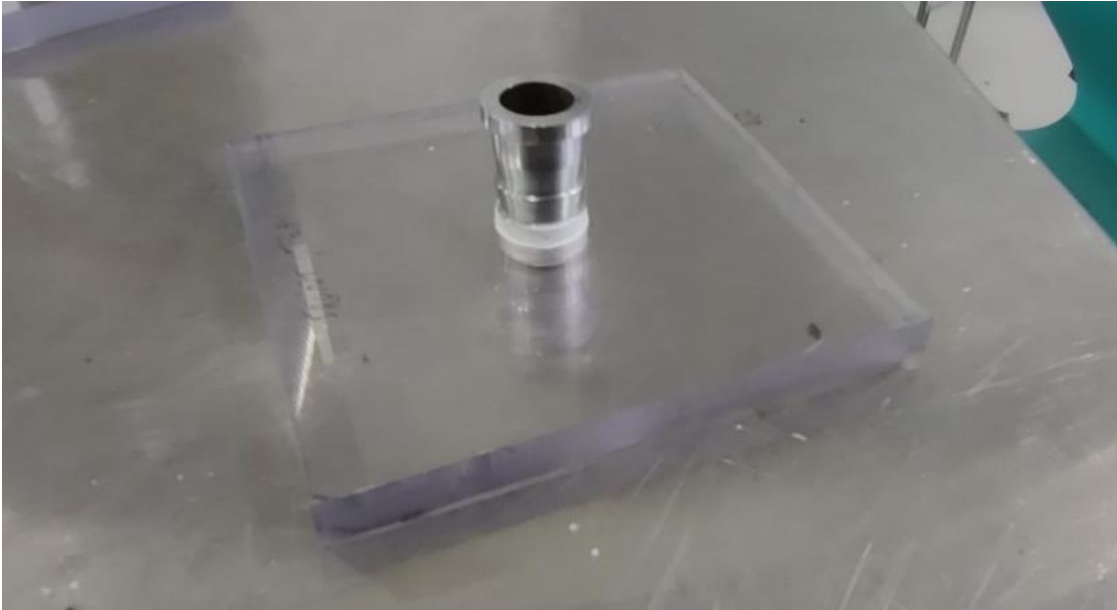
Practical arrangements: -

Supervision:
As a general rule, the student is entitled to 15-20 hours of supervision. This includes necessary time for the supervisor to prepare for supervision meetings (reading material to be discussed, etc.).

APPENDIX B: Hansen Coupling
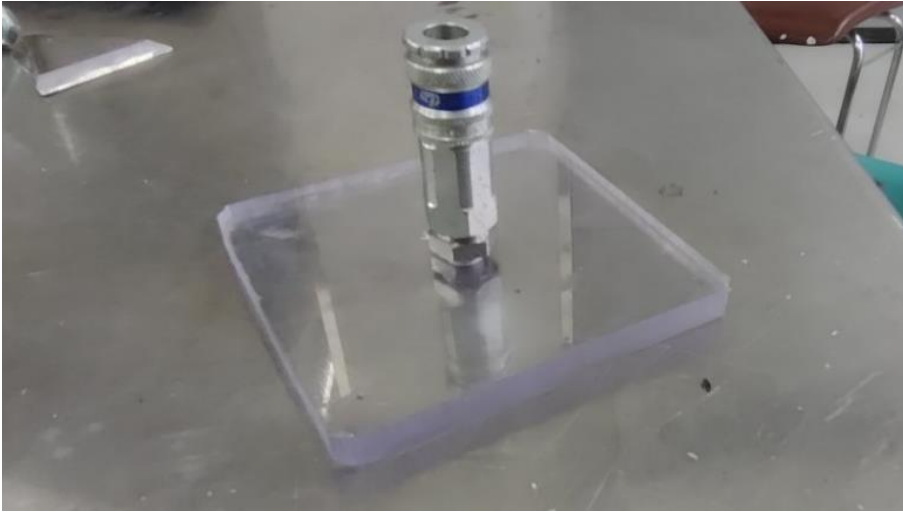
APPENDIX C: Exit plate, with pipe attachment

APPENDIX D: Simulation code, Tuned vs Untuned model code

```python
1  """
2  Created on Wed May 25 02:14:39 2022
3
4  @author: Suraj
5  Remark: comparison of tuned vs untuned model
6  """
7
8  import numpy as np
9  import math as mth
10 from scipy.integrate import odeint
11 import matplotlib.pyplot as plt
12
13 #function that returns the value dDdt
14 def model (D1,t):    #tuned model
15     k = 0.598
16     pi= 3.1415
17     h_fg = 4180
18     v = 2.2
19     C_p = 2
20     C = 1
21     Tb = 100
22     T0 = 17
23     rho = 997
24     myu = 0.5
25
26     Re = 2000
27     Pr = 1.5
28
29     dT = 2284   #2384-100
30
31     z = 0.4*(Re**0.5)*(Pr**(1/3))
32
33     nu = -4*k*dT*((1/C)+z)
34     de = rho * (C_p*(Tb-T0) + h_fg)
35     dDdt = nu/de
```

```python
36
37     print (dDdt)
38     return dDdt
39
40
41 #function that returns the value dDdt
42 def unmodel (D1,t): #untuned model
43     k = 0.598
44     pi= 3.1415
45     h_fg = 4180
46     v = 2.2
47     C_p = 2
48     C = 1
49     Tb = 100
50     T0 = 17
51     rho = 997
52     myu = 0.5
53
54     Re = 2000
55     Pr = 1.5
56
57     dT = 2284   #2384-100
58     z = 2 + 0.4*(Re**0.5)*(Pr**(1/3))
59
60     nu = -4*k*dT*z
61     de = rho * (C_p*(Tb-T0) + h_fg)
62     dDdt = nu/de
63
64     print (dDdt)
65     return dDdt
66
67 """
68 calling the function and initializing values
69 """
70 #initial condition
71 D0 = 0.005
```

```
72
73 #time points
74 t = np.linspace (0,.2,50)
75
76 #solving ODE
77 tuned = model
78 untuned = unmodel
79 D1 = odeint(tuned,D0,t)
80 D2 = odeint(untuned,D0,t)
81 #Dr = odeint(ranzmodel,D0,t)
82
83 #plot results
84 plt.plot(t,D1)
85 plt.plot(t,D2)
86 #plt.plot(t,Dr)
87 location = 0
88 legend_drawn_flag = True
89 plt.legend(["tuned","untuned"], loc = 0, frameon = legend_drawn_flag)
90 plt.xlabel('Time (in seconds)')
91 plt.ylabel('Square of Droplet Diameter (in metres)')
92 plt.show()
```

APPENDIX E: Simulation code, rate of droplet evaporation with droplet diameter

```python
"""
Created on Wed Apr 13 13:00:36 2022

@author: Suraj

Remark: effect of droplet diameter on rate of change of droplet
diameter
"""

import numpy as np
import math as mth
from scipy.integrate import odeint
import matplotlib.pyplot as plt

dxdt=[]

for i in range(50,1001,50):
        pie = 3.1415
        rho = 1000
        h_fg = 2260000
        T_flame = 2348
        T0 = 17
        Re = 800
        Pr = 3
        C_p= 1.2
        Tb = 100
        k = 0.18
        C = 0.5
        dT = 2248
        D = i
        z = 0.4*(Re**0.5)*(Pr**(1/3))

        nu = -2*k*dT*((1/C)+z)   #numerator
        de = rho*D*(C_p*(Tb-T0) + h_fg) #denominator
        dDdt = nu/de
        dxdt.append(dDdt)
        print (dDdt)


'droplet diameter, x axis'
d = np.linspace (50,1000,20)
#print(t)

print(d)
#plot results
plt.plot (d,dxdt,'r-')
plt.xlabel('droplet diameter, in microns')
plt.ylabel('dD/dt')
plt.legend(['x(t)'])
plt.show()
```

APPENDIX F: Simulation code, relation between velocity of the droplet and time

```python
"""
Created on Sat Apr 30 12:08:08 2022

@author: Suraj
Remark: Relation between velocity and time
"""

import numpy as np
import math as mth
from scipy.integrate import odeint
import matplotlib.pyplot as plt

def s_laminar():
    a = 2.96
    return a

def model(v,t):
    g = 9.81
    rho_p = 1000
    rho_f = 1.225
    D = 500*10**-6
    Cd = 0.47
    dvdt = (g*(rho_p - rho_f)/rho_p) - ((3*rho_f*Cd*v*v)/(4*D*rho_p))  #equation
    return dvdt


#initial velocity
v0 = [0 ,0 , 0, 3.5]
v0[1] = s_laminar()        #replacing second value with laminar velocity
v0[2] = 0.85 * s_laminar()  #fractional velocity
        #replacing third value
print (v0)
```

```python
34
35
36 #time points
37 t = np.linspace (0,1,50)
38
39 #solving ODE
40 v = odeint(model,v0,t)
41
42 #plot results
43 plt.plot(t,v)
44 plt.xlabel('time')
45 plt.ylabel('velocity')
46 location = 0
47 legend_drawn_flag = True
   plt.legend(["vel = 0 m/s","vel = 2.96 m/s (lam vel)","vel = 2.516
   m/s","vel = 3.5 m/s (reference)"], loc = 0, frameon =
   legend_drawn_flag)
   plt.show()
```

APPENDIX G: Simulation code, terminal velocity vs droplet diameter

```python
"""
Created on Wed Apr 13 13:00:36 2022

@author: Suraj
Remarks: terminal velocity vs droplet diameter
"""

import numpy as np
import math as mth
from scipy.integrate import odeint
import matplotlib.pyplot as plt

dvdt=[]
#The rate of change of diameter of the droplet due to heat transfer
def terminalvelocity (D):
        g = 9.81
        rho_p = 1000
        rho_f = 1.225
        D0 = D*10**-6
        print (D0)
        Cd = 0.47
        nu = 4 *g *D0 *(rho_p - rho_f)

        de = 3 *Cd*rho_f

        k = nu/de
        dvdt = mth.sqrt(k)
        print (dvdt)

        print (k)

        return dvdt

for i in range(500,2501,50):
    res=terminalvelocity(i)
```

```python
36      dvdt.append(res)
37
38 #droplet diameters
39 t = np.linspace (5,100000,41)
40
41
42 #plot results
43 plt.plot (t,dvdt,'r-')
44 plt.xlabel('droplet diameter, in microns')
45 plt.ylabel('terminal velocity, in m/s')
46 location = 0
47 legend_drawn_flag = True
48 plt.legend(["terminal velocity vs droplet diameter"])
49 plt.show()
```

APPENDIX H: Experimental result data sheet from Perimeter stand point

	Perimeter			Diameter			Average
	100	125	150	100	125	150	
25 mm with nozzle	132.74	140.608	132.27	21.12685	22.37912	21.05205	21.51934
25 mm without nozzle	115.385	114.017	111.265	18.36463	18.1469	17.7089	18.07348
50 mm with nozzle	146.791	145.487	139.512	23.3632	23.15566	22.20468	22.90785
50 mm without nozzle	120.569	121.2062	113.998	19.18972	19.29113	18.14388	18.87491

APPENDIX I: Improved mixing chamber model, with metal housing and bolt fitting for modularity